TURBULENCE WITHIN THE SURFACE BOUNDARY LAYER

A Dissertation

by

MOHAMMAD BARZEGARPAIINLAMOUKI

BS, University of Mohaghegh Ardabili, 2008
MS, Amirkabir University of Technology, 2011

Submitted in Partial Fulfillment of the Requirements for the Degree of

DOCTOR OF PHILOSOPHY

in

COASTAL AND MARINE SYSTEM SCIENCE

Texas A&M University-Corpus Christi
Corpus Christi, Texas

August 2021

© Mohammad BarzegarPaiinLamouki

All Rights Reserved

August 2021

TURBULENCE WITHIN THE SURFACE BOUNDARY LAYER

A Dissertation

by

MOHAMMAD BARZEGARPAIINLAMOUKI

This Dissertation meets the standards for scope and quality of
Texas A&M University-Corpus Christi and is hereby approved.

Darek Bogucki, PhD
Chair

Barbara Szczerbinska, PhD
Co-Chair

Fiqin Xie, PhD
Committee Member

Toshiaki Shinoda, PhD
Committee Member

Devanayagam Palaniappan, PhD
Committee Member

Anita Reed, PhD
Graduate Faculty Representative

August 2021

ABSTRACT

The ocean covers approximately 71 percent of the earth surface. The understanding of turbulence distribution and its role in the surface water and ocean mixing is vital in studying ocean processes such as: heat flux across the ocean interface and momentum flux as well as gas transfer and biogeochemical processes. The scarcity of field data hinders turbulent kinetic energy dissipation rate (TKED), temperature dissipation rate (TD) universal parametrization within the upper ocean boundary layer, especially very near the surface. In this project, I investigated how TKED, TD, and surface heat fluxes vary at the surface boundary layer based on laboratory and field experiment. I have conducted laboratory experiments in the Air–Sea Interaction Saltwater Tank (ASIST) at the University of Miami. We try to simply simulate the ocean when the horizontal heat and eddy fluxes play a prominent role in the ocean, like the front. In the field experiment, the data were collected during the LAgrangian Submesoscale ExpeRiment (LASER) in the northern part of the GOM during the winter of 2016. LASER was undertaken by CARTHE (Consortium for Advanced Research on Transport of Hydrocarbons in the Environment) as a large scale study of oceanic surface lagrangian transport and dispersion. The R/V Walton Smith was used during LASER as a main mobile oceanographic and atmospheric sensor platform. As a part of the experiment, we have documented the presence of a submesoscale front generated by the interaction of cold Mississippi river water with continental shelf water, which may be affected by the warm loop current generated in the GOM.

DEDICATION

I would like to dedicate this work to my family for their never-ending love, support, and encouragement.

ACKNOWLEDGEMENTS

I would like to thank my advisor, Dr. Darek Bogucki who provided me with immense support throughout my graduate school career. I would like to also thank my remaining committee member Drs. Barbara Szczerbinska, Feiqin Xie, Toshiaki Shinoda, and Devanayagam Palaniappan for their guidance and support. I am also indebted to Dr. Brian Haus, Mingming shao, Sanchit Mehta, Francis Lariji, Justin trull, and Shelby Metoyer and all other staff of the Rosential School of Marine and Atmospheric Science.

I would also like to acknowledge that this research has been supported by the Gulf of Mexico Research Initiative through the Consortium for Advanced Research on Transport of Hydrocarbons in the Environment under the grant NSF1434670.

TABLE OF CONTENTS

LIST OF FIGURES

FIGURES PAGE

LIST OF TABLES

TABLES PAGE

CHAPTER 1: INTRODUCTION-TURBULENCE

There are many opportunities to observe the turbulence surrounding us. Most flows occurring in nature and engineering applications are turbulent. The water in a river and channel; the smoke from a chimney, the earth-atmosphere boundary layer; the jet streams in the upper troposphere, and the airflow around aircraft wings, car, and ship are turbulence. The wake of the earth in the solar wind, the combustion processes, the flow behind the grid, and the current in the ocean are turbulent. The turbulence cause us to have an awkward trip when the aircraft experience air turbulence; however, it can be useful when you use turbulence to mix the sugar on your coffee. As the universe is a highly turbulent place, we need to understand the manner of turbulence flows.

1.1. Turbulence

The first difficulty in dealing with the turbulence is finding a formal and adequate definition of the turbulent flow. Since it is difficult to give a precise definition to the turbulent flow, all we can do is to list its characteristic attributes. The turbulent flow is characterized by irregularity, diffusivity, large Reynolds number, vorticity, and dissipation. An essential feature of the turbulence is its irregularity or randomness of the flow. Flow is random when the fluid velocity field varies irregularly and significantly in both time and position. The turbulence diffusivity causes rapid mixing and spreads the velocity fluctuation through the flow. The turbulent flow is characterized by a nondimensional parameter known as the Reynolds number, $R_e = UL/\nu$, where U is the flow speed, L is a characteristic length scale of the flow, and ν is the kinematic viscosity of the flow. Turbulent flows usually are generated at high Reynolds number, for example, in the pipe-flow

experiment, if the Re is higher than 4000, the flow is turbulence, and if it is below 2300, the flow is laminar (Pope 2001). Turbulent flow is characterized by a high level of three-dimensional vorticity fluctuations, and the turbulence has non-zero vorticity, that is, $\vec{\omega} \equiv \vec{\nabla} * \overrightarrow{U}$is non zero. The rotational flow is associated with different eddies size that the biggest one has most of the energy of the flow. The interaction among the various size of the eddies causes the energy passes from the larger scale to smaller ones, which is called the cascade process. In the smallest eddies, the energy is dissipated through viscosity to heat (Thorpe 2007), which is called Turbulent kinetic energy dissipation rate (TKED), ε.

1.2. Ocean turbulence

Turbulence is the dominant physical process in the ocean. In the ocean, turbulence plays a significant role in the surface process like surface heat flux (Pinker et al., 2014), gas transfer (Garbe et al., 2014 and Pereira et al., 2018), biogeochemical process (Michale et al., 2017), distribution and mixing of nutrients (Patterson et al., 1993), light propagation (Funk 1973), and resuspension of sediment in shallow waters (Kularatne and Pattiaratchi 2008).

Lamont and Scott (1970) observed that turbulence enhances the rate of gas exchange by renewing the surface mass content with small eddies. The eddies bring fresh water to the ocean surface where diffusion can happen and increase the gas exchange. Lamont and Scott (1970) related the gas transfer velocity K to the surface boundary layer turbulent kinetic energy dissipation rate as $k \propto (\varepsilon\vartheta)^{1/4}Sc^{-n1}$, where Sc is Schmidt number, and n1 vary between $\frac{1}{2}$ to $\frac{2}{3}$ based on the surface, the surface contamination. Moving fresh water to the surface by small eddies will increase the surface heat fluxes also. The turbulence sensible heat flux was calculated by the $H = \rho c_p \overline{\theta w'}$ (Zielinski et

al., 2018), where ρ is density, c_p is specific heat and $\overline{\theta w'}$ is the covariance of the turbulent fluctuate on of temperature (θ) and vertical velocity (w'). Badgley (1966) observed that the heat exchange at the water surface without ice is intense, and the rate of heat transfer between air and ocean at open water is two orders of magnitude larger than mature ice.

Rothschild and Osborn (1988) expressed that the turbulence on the boundary layer is important for the encounter rate of aquatic microorganisms and their prey by bringing predators and prey close to each other. Rothschild and Osborn (1988) introduced the encounter rate, Z, of planktonic predator and their prey under turbulence condition as $Z = c\pi R^2(Ur^2 + Vs^2 + 2Wt^2)$, where C and Ur are the concentration and randomly directed behavioral motion of prey particles, R is the reactive distance, Vs is swimming velocity, and Wt is the root mean square turbulent velocity. However, turbulence brings nutrient-rich water into contact with plankton cells; they also transported plankton away from growth and production (Pearman et al., 2017 and Pecseli et al., 2019). The microorganism or plankton themselves are a crucial source of food for larger aquatic organisms like fish and whales. The distribution of plankton in the ocean boundary layer is related to the nature of turbulent in both directions (Platt 1972, Macias et al., 2013; and Michalec et al., 2020).

The turbulence eddies also can be important in the oil spill, like the Deepwater Horizon oil spill that is considered to be the largest marine oil spill affecting the environment intensely (Wang et al., 2016). By spilling oil into the ocean, a thin film of the oil spreads at the water surface. The turbulence can disintegrate the oil film into small oil droplets, and that way, the speed of diffusion increases (Hoult 1972 and Nissanka et al., 2018). The small droplet can be dispersed vertically in the water column by turbulent diffusion, and the larger oil droplet stays on the surface and contaminates the animals and shoreline.

1.3. Objective and Experiments

The turbulence at the ocean surface boundary layer plays a significant role in the air-sea gas exchange, biogeochemical cycles, and pollutant transport such as accumulation and subduction of carbon, heat, salt, and dissolved gasses, oil droplets, and phytoplankton from the ocean's surface to its interior. Research has been conducted pertaining to the turbulence within the ocean boundary layer. The paucity of field data and observing turbulence centimeters below the water surface hinders the universal parameterization of the turbulent kinetic energy dissipation rate (TKED) and temperature dissipation rate (TD) within the upper ocean boundary layer. In this research work, we present a set of laboratory and field experiments to investigate the variation of TKED and TD on the surface oceanic boundary layer under the different internal and surface forcings conditions. Due to the gaps in understanding the very near surface process in the field, the laboratory experiment could be a helpful way of understanding the boundary process in field conditions.

As controlling of the condition in the ocean field is difficult, the laboratory experiment was carried out in the Air-Sea Interaction Saltwater Tank (ASIST) at the University of Miami (Fig. 1). The tank was equipped with the heater grid and turbulence generating grid. The internal turbulence generates in the ASIST tank by passing water from the grids, and its combination with the surface convection and waves can be the simulation of the ocean in the lab. The data were collected by the VMP 200 (for more detail, look at Appendix F) with distance from the grid and at the top surface boundary layer, z=0 – 0.16 m. The results and detailed experimental method is explained in chapter 2.

(a)

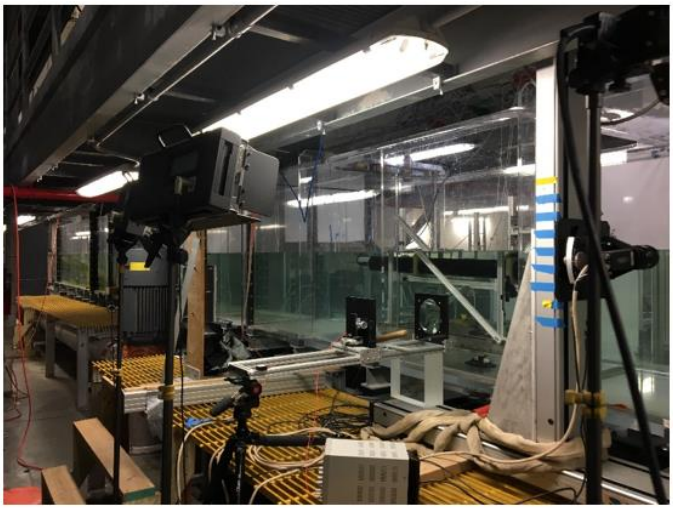

(b)

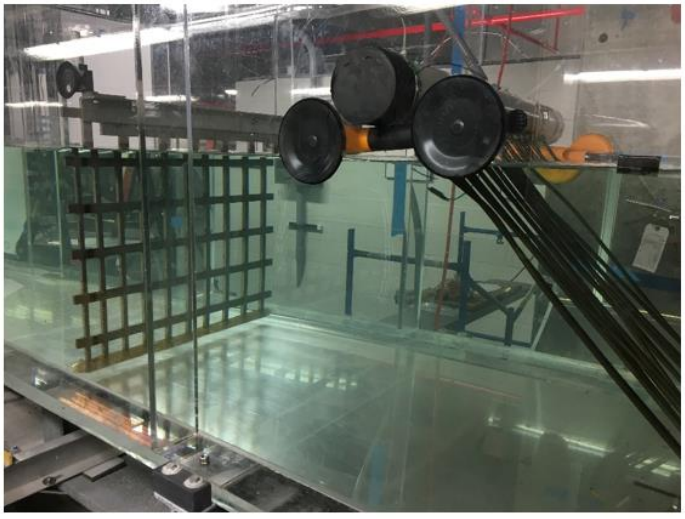

Fig. 1. The ASIST tank of the University of Miami equipped with heater grid and turbulence generating-grid. Data were collected by VMP and Current meter (Infinity-EM, Model AEM-USB).

The lab experiment gives us a general idea about the ocean process, and by having the general view about the turbulence within the boundary layer, we investigate the nature of turbulence on the oceanic boundary layer.

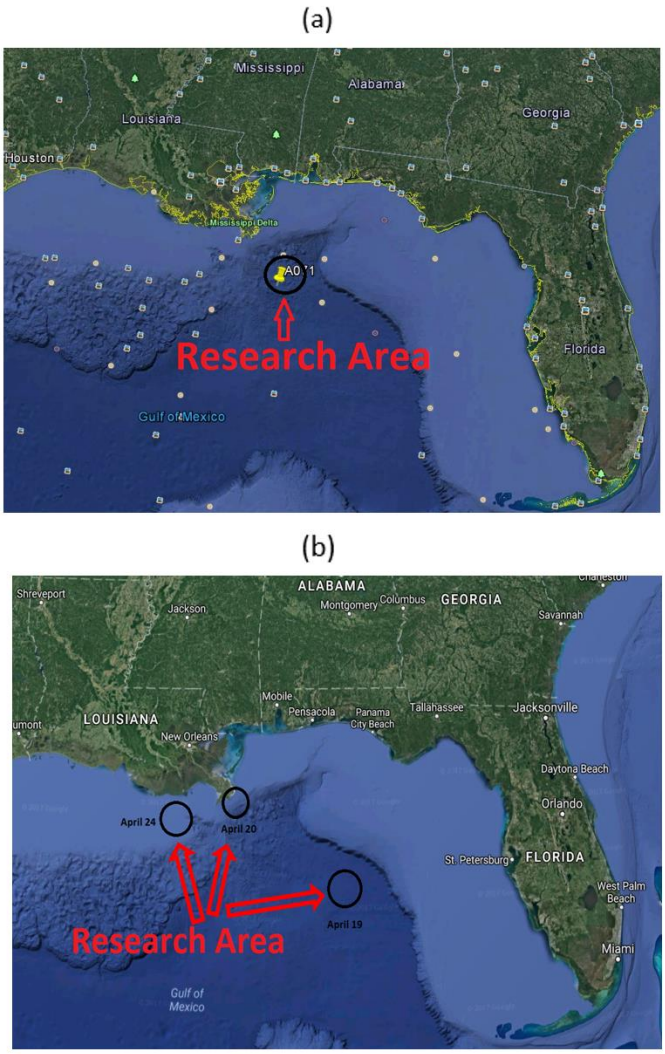

Fig. 2. The location of the LASER and SPLASH experiments in the Gulf of Mexico (www.google.com/earth).

The data used for our studying was collected during the LAgrangian Submesoscale ExpeRiment (LASER) in the northern Gulf of Mexico between 88.2˚-88.4˚W and 28.2˚- 28.3˚N during January 2016 and Submesoscale Processes and Lagrangian Analysis on the Shelf (SPLASH) between 86.3˚-90.3˚W and 27.5˚- 28.9˚N during April 2017.

The work days for the LASER and SPLASH experiments were as follows

For the LASER experiment

- January 29: 15:21 pm till 20:09 pm (UTC) -12 profiles (10 Up-cast)
- January 30: 16.21 pm till 21.02 pm (UTC) - 33 profiles (30 Up-cast)
- January 31: 16.24 pm till 20.14 pm (UTC) - 27 profiles (24 Up-cast)

And for the SPLASH experiment

- April 19: 15:07 pm till 17:11 pm (UTC) - 23 profiles (19 Up-cast)
- April 20: 18:55 pm till 21:49 pm (UTC) - 21 profiles (17 Up-cast)
- April 24: 17:26 pm till 1:20 am (UTC) - 24 profiles (24 Up-cast)

In this study, the high-resolution microstructure measurements were used from the LAgrangian Submesoscale ExpeRiment (LASER). The LASER was conducted to understand the submesoscale ocean currents in the northern part of the Gulf of Mexico, where the interaction of the Mississipi River plume and continental shelf waters create multiple submesoscale fronts. The water in the Mississipi side was cold and vertically stratified (CVS); however, the water was warm and horizontally stratified (WHS) on the other side of the front. In this experiment, we have investigated how the TKED, TD, surface heat fluxes, and turbulent heat fluxes change across the front. In chapter 3, we present the results of the turbulence process across the front.

CHAPTER 2: THE RESPONSE OF THE WATER SURFACE LAYER TO INTERNAL TURBULENCE AND SURFACE FORCING

2.1. Abstract

The aim of this research is to experimentally study how the turbulent kinetic energy dissipation rate (TKED or ε) and temperature dissipation rate (TD or ε_θ) change within the surface boundary layer of a grid generated turbulent flow. In our experiment, the minimum turbulence Reynolds number, Re_λ, calculated based on the Taylor microscale, λ,was Re_λ= 487 for the mean water flow velocity of 0.066 m/s.

We have carried out an experimental study of the turbulence kinetic energy dissipation rate (TKED or ε) and temperature dissipation rate (TD or ε_θ) within the water surface layer in the presence of internal turbulence, nonbreaking wave, and surface convection.

We noted that the nonbreaking wave dominates the TKED values within the surface layer. While analyzing the vertical TKED variability, the presence of a wave affected layer from the water surface to a depth of $z \approx 1.25\ \lambda_w$ is observed, where λ_w is the wavelength. The TKED associated with nonbreaking waves ε ranged to $4.9 \times 10^{-6} - 7 \times 10^{-6}$ m^2/s^3 for the wavelength range of 0.038 m < λ_w< 0.098 m categorized as the gravity and gravity-capillary wave regimes (Munk et al., 1951, Laxague et al., 2016, Chen et al., 2016).

The TKED values increases for longer λ_w and nonbreaking wave TKED values represent their significant contribution to the ocean energy budget and dynamic of surface layer considering that it covers the large fraction of surface wave (Bogucki et al., 2020, Anguelova et al., 2006}. We also found that the surface mean square slope (MSS) and wave generated TKED have the same order

of magnitude, i.e., MSS ~ε. Besides, we have documented that the small-scale temperature fluctuation change (TD) is consistent with the large-scale temperature gradient change (d<T>/dz). The value of the THF is approximately constant within the surface layer. It represents that the measured THF near the water surface can be considered a surface water THF, challenging to measure directly.

The power-law decay for temperature variance, $< \theta^2 > \sim x^{-m}$ where x is the distance from the grid, equals m=1.13, and for TD, $< \varepsilon_\theta > \sim x^{-(m+1)}$ equals m=1.25. The power-law decay for TKED, $< \varepsilon > \sim x^{-(n+1)}$, equals 1.01<n<1.18 for different mean velocities. Our observations indicate in addition to the grid-generated turbulence and heater grid, there are other spatially distributed sources of temperature and energy variance within the tank.

2.2. Introduction

The ocean covers approximately 71 percent of the earth surface. The understanding of TKED distribution and the TKED role in the surface water and ocean mixing is vital in studying ocean processes such as: heat flux across the ocean interface (Pinker et al. 2014) and momentum flux as well as gas transfer and biogeochemical processes (Pereira et al. 2018, Garbe et al. 2014 and Hicks et al. 1976). At the air-sea interface, the exchange of heat, moisture, momentum and gas transfer is carried out by molecular transfer processes, but away from the surface, at a depth greater than~1mm, the turbulence dominates the mixing processes (Dourado and Oliveira 2001).

The TKED can be found from the relationship $\varepsilon = 2\nu < s_{ij}s_{ij} >$ (Pope 2001), where s_{ij} is the fluctuating rate of strain: $s_{ij} = \frac{1}{2}(\frac{\partial u_i'}{\partial x_j} + \frac{\partial u_j'}{\partial x_i})$. Here ν is the kinematic molecular viscosity, i and j=1, 2 and 3, u_i' represents the fluctuating part of the velocity components in the x, y, and z-

directions, respectively and < > is the ensemble average. The rate of temperature dissipation TD or ε_θ, comes from the equation $\varepsilon_\theta = 2K_\theta < (\frac{\partial \theta}{\partial x_i})^2 > = 2K_\theta < (\frac{\partial \theta}{\partial x})^2 + (\frac{\partial \theta}{\partial y})^2 + (\frac{\partial \theta}{\partial z})^2 >$ (Pope 2001), where K_θ is the thermal molecular diffusivity, and θ is the fluctuating part of temperature.

The vertical TKED (Sutherland et al., 2013) and the rate of the TD variability (Bogucki et al., 2015) have been investigated within the upper ocean boundary layer while the boundary layer influenced by the surface forcing such as heat flux (Fredrikson et al., 2016), surface wave (Wang and Wijesekera 2018)), wind stress (Wuest et al., 2000) and internal sources of turbulence (Wain et al., 2015).

Fredriksson et al. (2016) simulated a numerical model to calculate the TKED for a free surface flow driven by natural convection. They found that the oceanic free convection results in a sharp change of TKED beneath the water surface. Wuest ei al. (2000) measured the TKED in the wind-forced stratified water, and observed that ≈90 % of turbulent kinetic energy was dissipated within the upper boundary layer. Terray et al. (1996) investigated the TKED under breaking waves, and observed a large uniform TKED from the surface water to a depth of $z=0.6H_s$, where H_s is the significant wave height. Babanin and Haus (2009) conducted a laboratory experiment to measure the TKED beneath monochromatic nonbreaking waves, which showed the presence of TKED.

Given that the percentage of the ocean surface covered by wave breaking under strong wind is less than 10 % (Anguelova et al., 2006), it indicates the significant role of the nonbreaking wave on the ocean budget. Babanin and Haus (2009) conducted a laboratory experiment to measure ε beneath monochromatic nonbreaking waves, which showed the presence of ε. Bogucki et al. (2020) observed that ε associated with nonbreaking solitary waves ranged to $\varepsilon \approx 3*10^{-4} m^2/s^3$ for a wave amplitude of 50 cm. The scarcity of field data hinders ε and χ universal parametrization

within the upper ocean boundary layer, especially very near the surface. This paper presents laboratory experiments in the Air-Sea Interaction Saltwater Tank (ASIST) at the University of Miami. We try to simply simulate the ocean when the horizontal heat and eddy fluxes play a prominent role in the ocean, like the Front in the Gulf of Mexico where the Missipi river with massive horizontal eddy fluxes reach the ocean and generate the Front (Barkan et al., 2017 and Bogucki et al., 2020). We investigate the THF, ε and χ variability very close to the air-sea interface, 0.5 cm beneath the water surface, when subject to the internal turbulence, surface convection, and nonbreaking wave categorized as the gravity and gravity-capillary wave regimes (Munk et al., 195, Laxague et al., 2016 and Chen et al., 2016). The sources of turbulence and temperature flux in our experiment and the experimental setup, are addressed in section 2. Section 3 describes the experimental results , ε, χ, and THF. Finally, a conclusion is given in section 4.

2.3. Experimental setup, data acquisition and analysis

We simulated the oceanic-like forcing in our laboratory experiment by having the three turbulence sources, i.e., the internal sources of turbulence, surface convection, and nonbreaking surface waves.

2.3.1. Experimental setup

The experiments were conducted in the ASIST tank at the University of Miami, equipped with the turbulence generating grid and a heated-grid (Figure 3). The tank walls are constructed of acrylic panels with a thickness of 0.024 m and have dimensions 15 m long, 1 m wide, and 1 m high. In our experiment, we analyzed data for the mean water flow velocity of $\langle U \rangle$ = 0.066 m/s, 0.125 m/s, 0.167 m/s, and 0.183 m/s. The heated-grid was located at the tank entrance, and the

turbulence-generating grid was mounted 0.5 m behind the heater. The freshwater depth during the experiment was kept constant, d_t= 0.5 m. The thickness of the bar of the grid was d_b =0.02 m, and the distance between the centers of two cells on the grid horizontally and vertically was M= 0.1 m. The solidity of the grid was $\sigma = 0.36$ (Murzyn et al., 2005).

The grid Reynolds number was given by $Re_M = \frac{\sigma M<U>}{\nu}$ (Grzelak and Wiercinski 2005) in our experiment which equals to Re_M = 2366, 4482, 5988 and 6630 for the velocity of $< U >$ = 0.066 m/s , 0.125 m/s, 0.167 m/s, and 0.183 m/s, respectively. The minimum turbulence Reynolds number, $Re\lambda = \frac{<u_i'>_{rms}}{\nu}\lambda$, calculated based on the Taylor microscale, $\lambda \approx \sqrt{\frac{15\nu}{\varepsilon}} < u_i' >_{rms}$, was 487 for mean water flow velocity of 0.066 m/s, where $< u_i' >_{rms}$ is root mean square of the velocity fluctuation (Tennekes et al., 1972). The flow velocity was measured with a current meter (Infinity-EM, Model AEM-USB) with a sampling rate of 10 Hz. The Rockland Scientific vertical microstructure profiler (VMP200) (Lueck et al., 2002, Macoun et al., 2004, Lueck et al., 2010 and Lueck2013) was used to measure the ε and χ with a sampling rate of 512 Hz. The VMP200 was equipped with two shear sensors that the sensors sampled the small-scale shear component.

The shear probe, called the airfoil probe, was initially developed for the wind tunnel work (Siddon et al., 1965), and Osborn (1980) adopted it for oceanic measurements. The shear probe senses velocity fluctuations cross-stream to its travel direction. The VMP200 was also equipped with a fast thermistor FP07. The response time of the thermistor FP07 is 7 ms in water for the speed of 1 m/s (Lueck et al., 2013). The speed increase causes the decrease of thermistor response time. The temperature resolution of the FP07 is 0.0001 C. The measured temperature temporal gradients $\frac{\partial\theta}{\partial t}$ via Taylor's frozen hypothesis to $\frac{\partial\theta}{\partial x} = \frac{1}{<U>}\frac{\partial\theta}{\partial t}$. The VMP was mounted horizontally in the tank

(Figure 3), and it collected a time series of the velocity shear and temperature at a depth range of 0.5 cm $< z < 25$ cm. By considering the standard assumption that the oceanic flow can be approximated by idealized homogenous and isotropic turbulence, the ε values were calculated by the VMP200 measured shear spectrum $\psi(K)$ as (Lueck et al. 2002):$\varepsilon \approx \frac{15}{2} \nu \int_0^\infty \psi(K) dK$, where K is the wavenumber, and ν is the kinematic viscosity. The shear probe's finite spatial size causes it to spatially average the smallest eddies for large K. The lost variance is corrected with a transfer function (Macoun et al., 2004). The shear spectrum is also fixed for the vibration-coherent portion by the Goodman et al.' technique (Goodman et al., 2006). Kolmogorov (Kolmogorov et al., 1991) derived the shear spectrum by assuming that the larges scales of turbulence are much larger than the Kolmogorov scale. Kolmogorov (Kolmogorov et al., 1991) presented that the shear spectrum is proportional to $K^{1/3}$ in the inertial subrange. Due to difficulties in resolving eddies scales smaller than the Kolmogorov length (Peterson et al., 2014), the shear spectrum can be fitted with an empirical turbulence spectrum such as the Nasmyth spectrum (Oakey et al., 1982 and Lueck et al.,2013) over the viscous and inertial subrange. The Nasmyth spectrum's integral over the wavenumber is considered as a ε value in this paper.

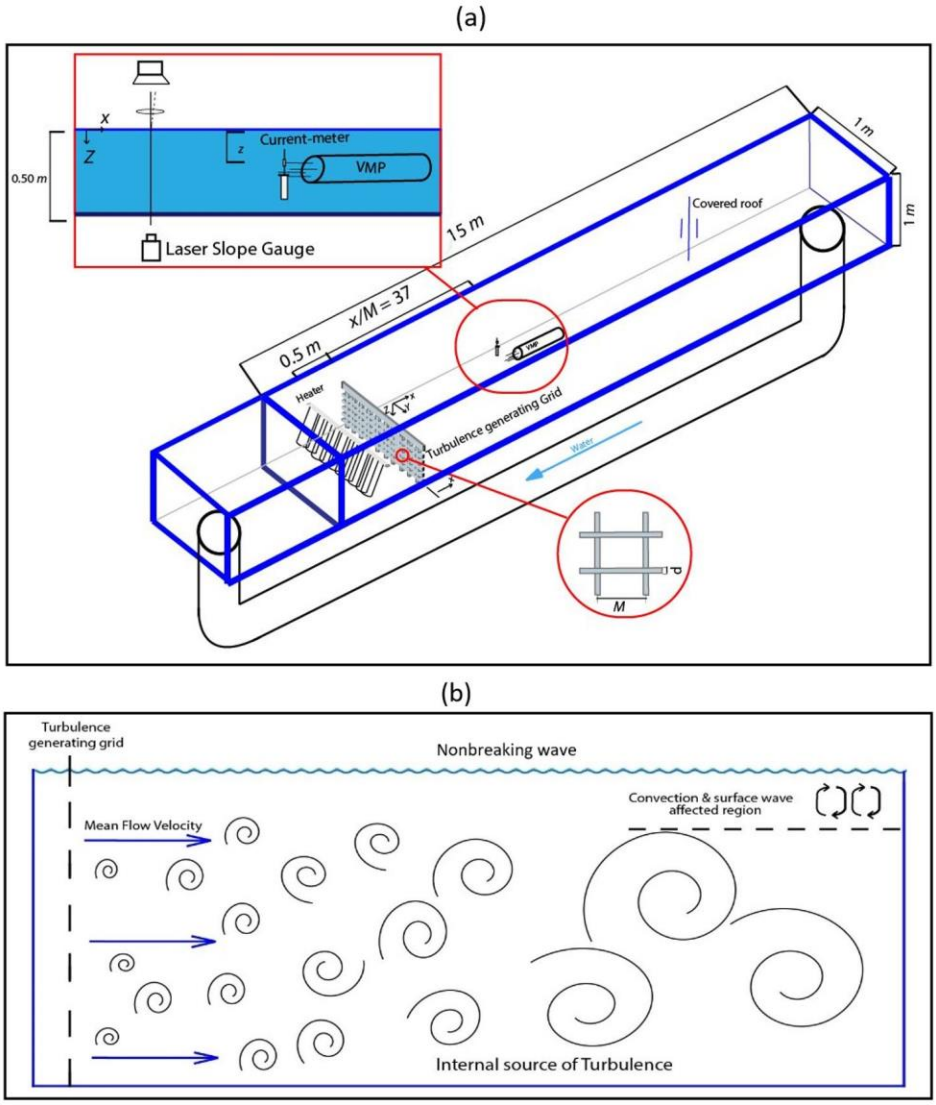

Fig. 3. (a) A schematic of the ASIST tank at the University of Miami. Heated-grid and grid generated turbulence were installed at the tank entrance. The vertical microstructure profiler (VMP), laser slope, and current meter locations from turbulence generating grid are shown by x/M. The insets indicate a side view of the instrument's vertical position at the tank with a fresh-water level of 0.5 m and the turbulence generating grid's mesh shape. (b) A schematic of internal and surface sources of turbulence. The blue arrows show the direction of the mean flow velocity. The swirl lines represent the background or internal turbulence generated by the grid.

The rate of temperature dissipation TD (or χ) can be obtained from the VMP measured one dimensional temperature gradient spectra, $\Phi(K)$, as (Bluteau et al. 2017): $\chi \approx 6\, K_\theta \int_0^\infty \Phi(K)dK$, where K_θ is the thermal molecular diffusivity. For measuring χvalues in this paper, we first find the fitting line for temperature gradient spectra along the dropping part of the spectrum. χ values were measured by multiplying $6K_\theta$ with the integral of the temperature gradient spectrum and fitting line along the wavenumber domain. A sophisticated thermistor signal processing, installed on the VMP200, minimizes the electronics noise. Therefore, the measured temperature spectra are only limited by the thermistor inertia (Lueck et al., 2002). When traveling through the water column is faster than 0.1 m/s, the thermistor (FP07) used in the VMP200 does not fully resolve the temperature variance of the temperature field (Lueck 1977), considering that we did not implement the thermistor spectral response function correction on the χ values \cite{lueck1977spectral} (Figure 3b). The correction of χ values is difficult because the thermistor's response time has been found to depend on the VMP velocity (Lueck et al., 1977) and thickness of the glass coating of the sensor tip (Nash et al., 1999) that varies for each individual thermistor. Nash et al. (1999) observed that only 1 % of the temperature gradient variance could be resolved at a profiler of 0.6 m/s for χ values larger than $1 * 10^{-6} C^2/s$. The VMP200-measured χ values are the underestimates of the χ for the mean flow velocity of faster than 0.1 m/s. The imprecise-measured values present the χ behavior within the surface layer, and due to that, we present χ values in this paper (Figures 3a and 4b).

The direction of the flow and the VMP probes generates an instantaneous angle of attack (see Appendix G). The angle of attack was one of the most critical parameters that could affect the VMP results. The effects of this angle on ε and χ results were investigated in the ASIST tank. The

shear and thermistor probe results were found to be consistent for an angle of attack <12 degree, with an error of about 10 % and 20 % for the shear and the thermistor probes, respectively. The angle of attack was kept less than 1 degree in experiment that gave an error of less than 2 %.

The nonbreaking waves were observed to be propagated and spread uniformly along the tank. We are unsure of the source of propagating waves; therefore, the generated-wave may not be entirely representative of the effects of actual ocean waves. We speculate that the surface stress created by the friction between the moving water and the stationary air contribute partially to generate a surface wave in addition to the grid. The sidewall also effects on the wave's generation for larger flow velocity.

<U> = mean flow velocity (m/s)	0.101	0.125	0.167	0.183
Re_M=(σ M <U>/ υ) = grid Reynolds number	2366	4482	5988	6630
MSS= Mean square slope	2.35×10^{-5}	6.2×10^{-5}	1.04×10^{-4}	1.23×10^{-4}
λ_w = wavelength (m)	0.038	0.051	0.074	0.098
$H = 2 < \eta >$ = wave height (m)	0.003	0.0034	0.0060	0.0068
ϵ_0 = background turbulence at x/M=37 (m^2/s^3)	1.5×10^{-6}	4.2×10^{-6}	1.05×10^{-5}	1.34×10^{-5}
B_0 = surface buoyancy flux (m^2/s^3)	1.70×10^{-8}	1.72×10^{-8}	1.74×10^{-8}	1.75×10^{-8}
L_0 = Oboukhov length scale (m)	1.24	1.22	1.2	1.16

Table 1. The table presents the wave parameters like wavelength and the wave height of the created surface wave for different mean flow velocities and the summary of the paper.

The laser wave slope instrument is used to measure the water surface slope, dη/dx (installed 1.35 m in front of the VMP). The η is the surface elevation that equals η=0.5H, where H is wave height. The point height/slope gauge consisted of an Argon-Ion (488 nm–blue) laser transmitting 2W of power whose beam was directed upward through the water surface. Above the tank along the sidewall, a line-scan camera observed the surface spot and tracked the vertical movement (Donelan

et. al., 2009). The surface slope spectrum P(K) is equivalent to K2S(K) where S(K) is the elevation spectrum of η, and the mean square slope is $MSS = \int_0^\infty K^2 S(K) dx$ (Elfouhaily et. al., 1997).

2.3.2. Internal source of turbulence

The internal source of turbulence, or pre-existing source of turbulence, in the ocean was simulated by the grid generated turbulence, which was created by passing water through a solid grid (Figure 3). The values of ε, χ, and temperature variance, $<\theta^2>$, decay with distance from the grid which are proportional to $\varepsilon \approx x^{-(n+1)}$, $\chi \approx \frac{n<U>B}{2} x^{-(m+1)}$, and $< \theta^2 > \approx (x)^{-m}$, respectively (Zhou et. al., 2000) (see Appendix A). The power-law exponent of m and n are to be determined empirically. Antonia et al. (1998) showed a value of n to be n=1.28, and more recently, Hearst and Lavoie (2014) found a value of n = 1.37 and 1.39 behind a square-fractal-element grid. Warhaft and Lumley (1978) found that the temperature decay rate varied over a wide range of 0.87<m<3.09.

2.3.3. Convection and turbulent heat flux

In the experiment, the mean water temperature at a depth of z= 0.15 m was <T>= 26.82 c (Figure 4) and the air temperature was <T>= 25.70 c at 0.2 m above the water surface. The heat transfer from the freshwater to air resulted in thermal convection in our experiment as salinity was approximately zero within the water depth. Convection affects the vertical transport of heat, momentum, and other properties. Despite their importance to ocean circulation within the upper ocean boundary layer (Soloviev et al., 2001), the vertical fluxes of heat and momentum are only

estimated indirectly. The turbulent heat flux (THF) was estimated as $\mathrm{THF} \approx \rho c_p < w'\theta >$ (Moum et. al., 1996), where ρ is water density and the c_p is water specific heat. We followed the Osborn and Cox (1972) approach to determine the value of turbulent temperature flux $< w'\theta >$. For the steady and homogeneous turbulence, by retaining only vertical dependence and by neglecting the surface wave for simplicity, the turbulent temperature flux is given by (Ruddick et. al., 1997) (see Appendix B):

$$< w'\theta > \frac{\partial <T>}{\partial z} = -K_\theta < (\nabla\theta)^2 > = -\frac{1}{2}\chi \quad (1)$$

The values of χ and temperature gradient $T_z = \frac{\partial <T>}{\partial z}$ were measured in our experiment, therefore, the value of the turbulent temperature flux can be estimated as $< w'\theta > = -\frac{1}{2}\chi/T_z$. Hence, the THF equation is rewritten as

$$\mathrm{THF} \approx \rho c_p \frac{\chi}{T_z} \quad (2)$$

2.3.4. Turbulence Scaling

Normalizing of ε aids in understanding which processes have significant effects on the surface layer turbulence (Esters et. al., 2018 and Fredriksson et al., 2016). The upper-ocean turbulence is predominantly generated due to atmosphere-ocean interaction by convection and surface wave (Esters et al., 2018). The base of our understanding of the vertical turbulence variability within the surface boundary layers in the ocean is mainly based on the turbulent flow studies over the solid wall-layer turbulence with the corresponding ''law of the wall'' (LOW), $\varepsilon = \frac{u^{*3}}{(kz)}$, where k=0.41 is von Karman's constant (Kitaigorodskii et. al., 1983 and Gargett et. al.,1989) and u^* is

friction velocity.is water-side friction velocity defined as $u_* = \sqrt{\tau/\rho}$,. Here τ is wind stress that assumes to be constant across air-sea interface so that $\tau = {u_*}^2\rho = {u_{*a}}^2\rho_a$, (Sutherland et. al., 2013), where u_{*a} and ρ_a are water-side friction velocity and air density, respectively. Terray et al.(1996) suggested enhanced values for ε relative to the LOW in the upper ocean, and we used their scaling method for wave-generated turbulence, ε_{wave} (see Appendix C). In addition to wave, the transfer of heat between water and air increases ε within the upper ocean boundary layer (Esters et. al., 2018) due to that the surface buoyancy flux, B_0, is used to investigate the surface convection role on turbulence (Fredriksson et. al., 2016 and Zahariev et al., 1997).

$$B_0 = -{c_p}^{-1}\rho^{-1}g\alpha Q + \rho^{-1}g\beta sE \quad (16)$$

Where g is gravity, α is the thermal expansion coefficient of water, β is the coefficient of salinity expansion, s is the surface salinity, and E is the evaporation rate.

2.4. Results and discussion

Two sets of experiments were conducted. The first set was to establish the power-law exponent of m and n. The data was collected at a depth of z= 0.25 m downstream of the grid-generated turbulence, 25< x/M<38, and at an equal distance from the horizontal sidewalls. In the second set of experiments, the data were collected within the surface boundary layer at a x/M =37 to clarify how the magnitudes of THF, χ, and ε change when approaching the water surface.

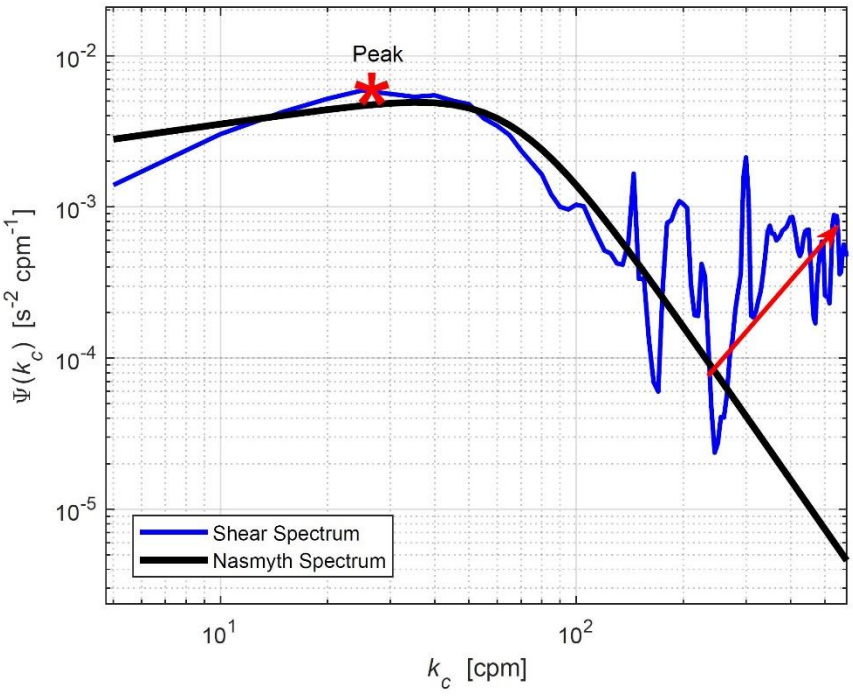

Fig. 4. Comparison of the Shear spectrum with Nasmyth spectrum for <U>=0.167 m/s at x/M=37 and depth of z=0.25 m. K_c is wave number in the unit of cpm that it equals to $K_c = K/(2\pi)$. The spectrum peak is shown with a red star, and the red arrow shows the rising part of the spectrum.

The data was collected between depths of 0.005 m< z < 0.17 m vertically and at an equal distance from sidewalls. The heater was set to the high setting (P_0=8.3 kW) when χ and ε were measured. As mentioned in section 2.1, χ and ε values are measured by temperature spectrum and empirical Nasmyth spectrum. Comparing the shear spectrum with the Nasmyth spectrum for <U>=0.167 m/s at x/M= 37 indicates an acceptable fitness between the graphs (Figure 4). The shear spectrum (see Appendix H)starts to rise at a wavenumber by a factor of 70 below its peak (Figure 4), which shows the spectrum contains more than 90 % of all shear variance as mentioned in Rockland scientific international note 28 (Lueck et. al., 2013).

This section uses four parts to represent the results of our experiment. Section 3.1 displays the power-law decay results and the modified grid-generated turbulence model. The changes in THF, χ , and ε within the surface boundary layer are presented in sections 3.2 and 3.3. Finally, the effects of nonbreaking waves on the near-surface ε are shown in section 3.4.

2.4.1. Steady and spatially decaying background turbulence-grid generated turbulence

The VMP200 (Lueck et. al., 2002) measured ε, χ, and temperature variance $<\theta^2>$ at a constant depth of z=0.25 m and selected distances along the tank centerline ($25<x/M<38$) for $<U>=0.183$ m/s. The data collected for $<U>=0.167$ were measured between $28<x/M<38$.

We estimated a background heat flux of about 25 w/m^2 from the equation of $Q \approx \left|(\rho c_p K_\theta \frac{\partial<T>}{\partial z})/A_w\right|$ (Wells et. al., 2009), where A_w is the water surface area. It likely changes during the experiments (The measured background heat flux is the summation of heat transfer from all sides of the tank walls and the water surface through the whole length of the tank).

The linear fitting line is used to find the power-law exponent for χ and $<\theta^2>$ that they were m=1.13 and m=1.25, respectively (Figure 3). We found that the power-law exponent for the decay of ϵ values was n= 1.04 and 1.16 for the flow velocities of 0.167 m/s and 0.183 m/s, respectively (Figure 3). Based on observed ε and χ in our experiment (Figure 3) and following Zhou et al. (Zhou et. al., 2000) and Bogucki et al. (2018) we found the following set of equations for χ and ε as a function of mean flow velocity $<U>$ and distance to turbulence-generating grid x:

$$\chi = 0.2 \frac{1}{<U>} P_0{}^2 \left(\frac{x}{M}\right)^{-2.13} \quad (3)$$

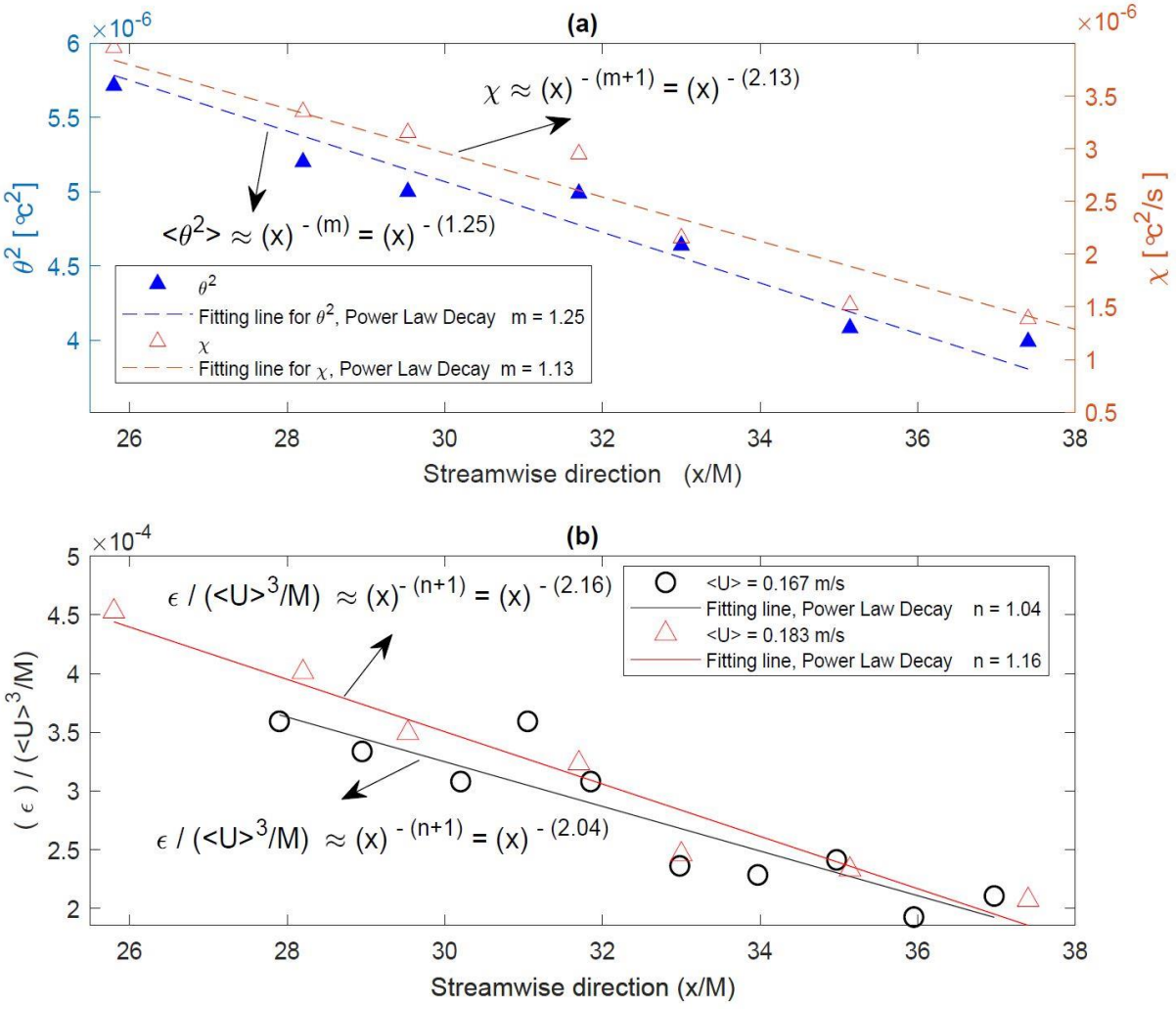

Fig 5. (a) Temperature variance (θ^2) and TD (ε_θ) values along the streamwise direction are shown. The dashed blue line and the brown line are the least-square linear regression of the θ^2 and ε_θ profiles, respectively. The mean flow velocity was <U>=0.183 m/s and the black arrow shows the reverse trend of the data resulting from the opening roof. (b) The normalized value of ε/(<U>^3/M) along the streamwise direction is shown. The black and red lines are fitting lines of the data for 0.167 m/s and 0.183 m/s, respectively. The data were collected at z=0.25 m. The heated-grid power was P_0=8.3 kW for both graphs of a and b. Also we can modify the grid generated turbulence by power-law decay exponent for TKED and TD (See Appendix D).

and

$$\varepsilon = 5 < U >^3 \ (\frac{x}{M})^{-2.1} \quad (4)$$

The set of equations are defined due to observed m and n in our experiment. The values are considered to be as m+1=1.13+1=2.13 for χ and the average of n+1=(1.04+1.16)/2+1=2.1 for ε .To have the χ in[c^2/s] and ε in [m^2/s^3], the <U> has to be expressed in [m/s]}, the P_0 in [W], and the factors of 0.2 and 5 have units of [mc^2/j^2], and [1/m], respectively.

2.4.2. Observations of free convective flow and associated vertical heat flux

Data was collected at x/M=36 where the tank roof was covered, and the air-water temperature difference was approximately uniform during the experiment. The average net surface vertical heat flux of $Q \approx |25| w/m^2$ in our experiment was not substantial in comparison to the mean range of net vertical heat flux in the ocean $Q \approx |150| w/m^2$ (Carton et al., 2018), and also the heated-grid generated a horizontal heat flux of $16.6\ kw/m^2$, which is smaller than the Kuroshio front region. The maximum Kuroshio current-caused horizontal heat flux is $\sim 6.2 * 10^4\ kw/m^2$ for a mixed boundary layer of $L_m = 35$ m (Pan and Sun 2018).

Fig. 6 depicts the vertical temperature, TD and vertical turbulent heat flux, and Fig. 6a depicts the vertical temperature profile. The temperature gradient increases near the water surface at a depth of z=0.028 m up to the water surface (Fig. 6a) due to the surface heat flux. The positive temperature gradient, due to the cooling of the water surface, results in the near-surface convection in our experiment.

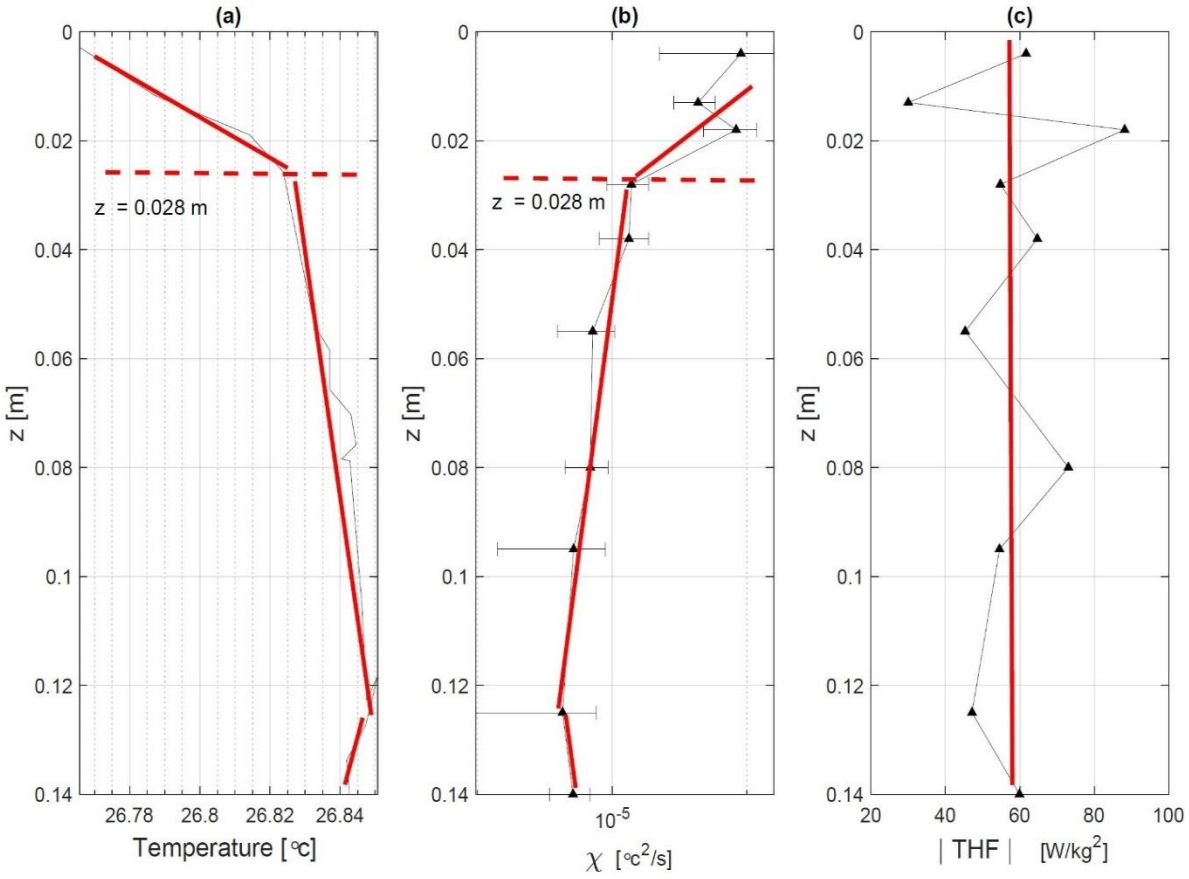

Fig. 6. (a) The vertical profile of temperature, (b) the vertical profile of TD rate (ε_θ) and (c) the vertical profile of turbulent heat flux $< w'\theta >= -0.5\ \varepsilon_\theta/(\partial T/\partial z)$ are depicted. The data for all three graphs were collected at a downstream distance of x/M = 36. The mean flow velocity is <U>=0.183 m/s and the heater has high-setting power. The dashed red lines show the depth that the change rate of the temperature gradient (a) and TD (b) vary. The red line is the fitting line of the graph. Note, the near-surface turbulent heat flux $< w'\theta >$ is approximately constant as denoted by the red line segment (c).

An appropriate normalization method is not identified for TD values; therefore, the TD values are depicted as an non-normalized values in Fig .6b similar to the Bogucki et al. (2015) and Peterson

and Fer (2014) works. Comparing Fig. 6a and 6b reveals that the change rate of TD varies when the temperature gradient changes. The value of TD increases by approaching the water surface (Fig. 6b) as the temperature gradient increases, which shows that the large scale vertical temperature gradient change, $< dT >/dz$, is consistent with the value of small scale temperature fluctuation, TD. The value of the vertical turbulent heat flux, $< w'\theta >$, can be found by dividing the value of TD, ε_θ, by the vertical temperature gradient, $< dT >/dz$, from Equation 2. The average of the THF values (the red line shows it in Figure 4c) are approximately constant within the surface layer; however, the THF's variance increases up to 50 % at 0<z<0.028 m, which is in the range of the wave-effected layer (see Fig. 5c).

2.4.3. Vertical TKED profile observations

The data was collected at x/M=37 from a depth of z=0.17 m up to z=0.005 m to investigate the vertical TKED profile. Scaling of the TKED aids in understanding and describing the physics of the boundary layer (Figure 7). The TKED is normalized by the grid-generated TKED called "background turbulence" ε_0 (Figure 7a). The surface buoyancy flux B_0 (Equation 3) and the wave-generated TKED ε_{Wave} (Equation 5) is also used to normalize the TKED (Figures 7b and c).

The ε_0 was measured at the tank center (z=0.25 m). The background turbulence ranges between $\varepsilon_0 \approx 0.5 - 3 \times 10^{-5} m^2/s^3$ that are within the subset of ocean TKED range, $\varepsilon \approx 10^{-11} - 10^{-3}$ m^2/s^3 (Mcmillan et al., 2016, Lozovatsky et al., 2017, Evans et al., 2018). The normalized TKED with background turbulence for different velocities converge together in deeper water; however, they diverge by approaching the water surface (z>0.02 m).

In Figure 7b, the TKED values ε are normalized with the summation of the surface buoyancy flux B_0 and background turbulence ε_0., i.e., $\varepsilon/(\varepsilon_0 + B_0)$ (Figure 7b). The Obukhov length scale L_0 (Soloviev et al., 2001) is used to normalize the water depth (Figure 7b), which characterizes the relative importance of the shear and buoyant convection in the boundary layer (Markowski et al., 2019, Soloviev et al., 2001). Given that the air temperature, humidity, and water temperature did not change during the experiment, the change of the surface buoyancy flux B_0 for the mean flow velocity range of 0.066 m/s to 0.183 m/s was small ≈2.8 % (Table 1). The similar rates for both scaling methods (Figures 7a and b) suggest that the background turbulence is larger than the turbulence generated with the surface convection, and the convergence of $\varepsilon/\varepsilon_0$ in depth indicates the dominance of the grid-generated turbulence.

The nonbreaking surface wave is another source of turbulence in addition to the surface convection. The doppler shifting correction (Drennan et al., 1994, Collins et al., 2017), was performed on the surface elevation spectrum and graphed in Figure 8a for the mean flow velocity of <U>=0.125 m/s, which represented the presence of the surface waves. In addition to the surface elevation spectrum, the visual observations show that the uniform surface waves are created along the whole tank when the water moves along the tank with the grid (Figure 8b) and without the grid (the figure does not show) inside the tank.

The wavenumber of elevation spectrum peak, K_max (Figure 8a), is considered to calculate the wavelength λ_w of nonbreaking waves. The wavelength ranges between 0.038 m < λ_w<0.098 (Table 1) categorized as the gravity or gravity-capillary regimes (Laxague et al., 2016). The integration of elevation spectrum S(K) gives the $<\eta^2> \approx \int_0^\infty S(K)dK$ (Elfouhaily et al., 1997), hereupon the wave height H = 2< η >

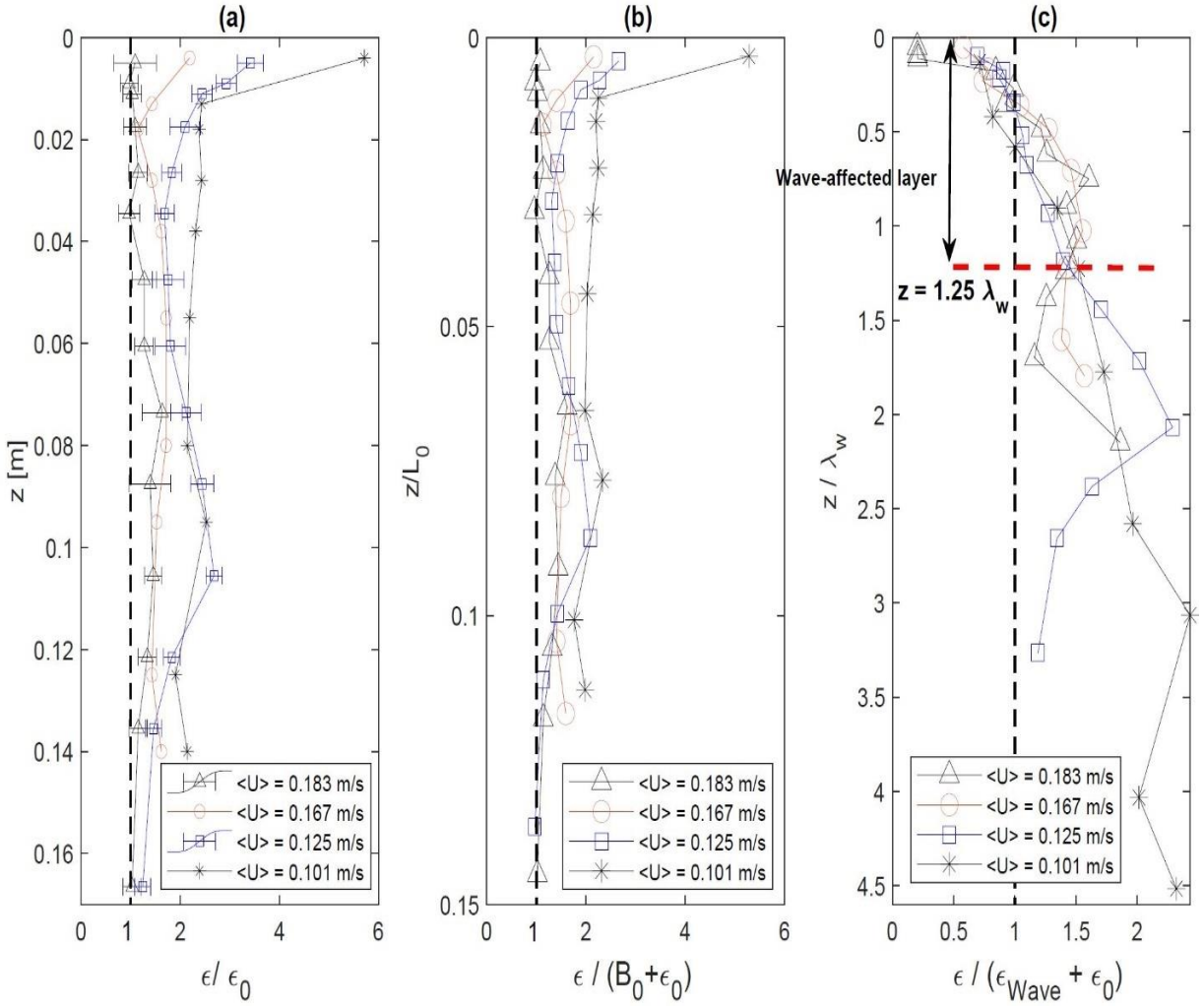

Fig. 7 The vertical profile of ε at the downstream distance of x/M = 37 for the mean flow velocity range of 0.101 m/s< <U> < 0.183 m/s are shown. The data was measured at a depth of z= 0.005 m to 0.17 m. (a) The ε is normalized by the background, or internal, TKED generated by the grid, ε_0 with associated error bars. (b) The ε is normalized by the summation of surface buoyancy flux, B_0, and background TKED, ε_0. (c) The ε is normalized by the summation of wave generated TKED, ε_{wave}, and background TKED, ε_0. The wave affected layer is presented with the dashed red line.

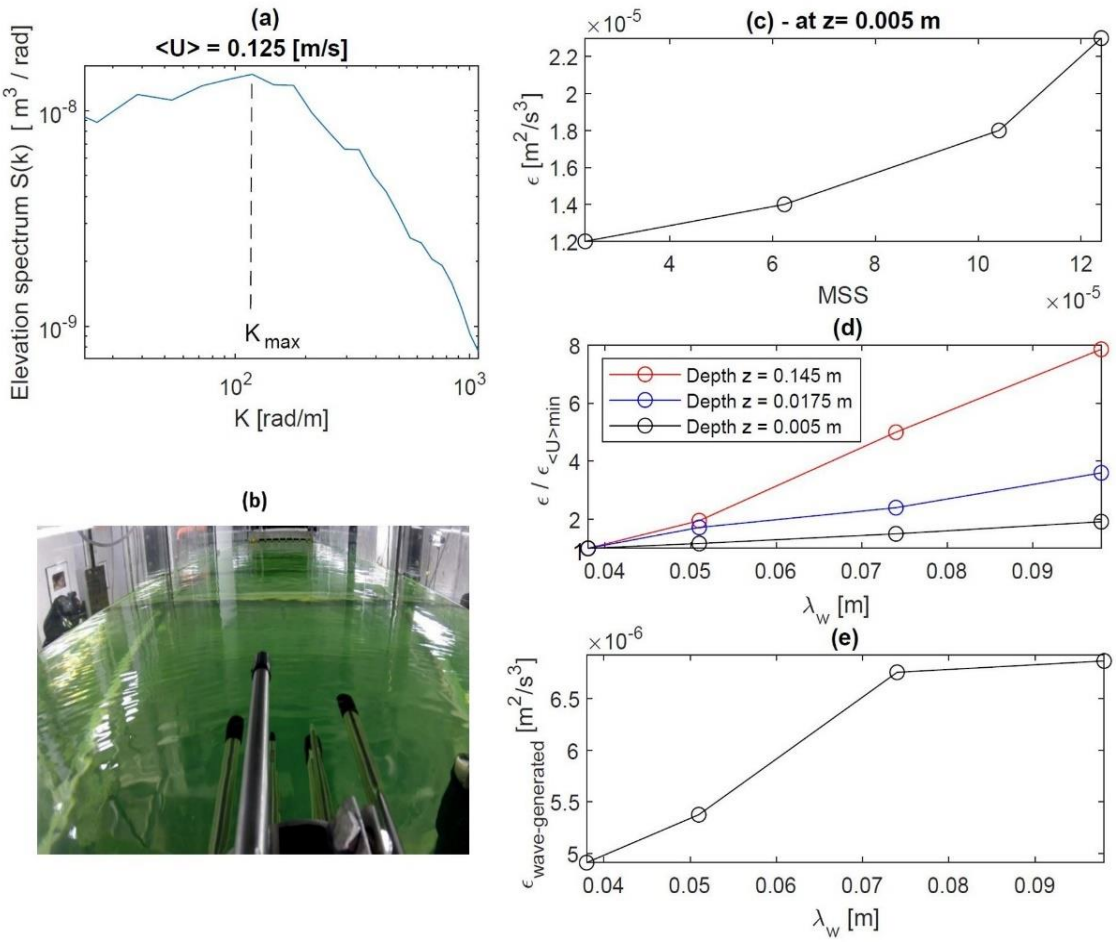

Fig. 8 (a) The surface elevation spectrum for the mean flow velocity of <U>= 0.125 m/s is shown. The wavenumber related to the spectrum peak is shown by K_max. (b) The nonbreaking surface wave generated for <U>=0.125 m/s while the grid is located inside the tank. (c) The TKED change for different MSS is depicted at a depth of z=0.005 m. (d) The normalized TKED value of different flow velocities is shown at three depths. The TKED values are normalized with the TKED of the lowest mean flow velocity of each depth, $\varepsilon_{<U>\min}$. (e) The subtraction of the averaged-TKED within the wave-affected layer, $\varepsilon_{1.25\lambda_w}$ from the background TKED, ε_0, is considered as the wave-generated TKED, $\varepsilon_{\text{wave-generated}} = \varepsilon_{1.25\lambda_w} - \varepsilon_0$. The data were collected at the downstream distance of x/M = 37.

The TKED values normalized with the summation of the wave-generated turbulence ε_{Wave}, Equation C9, and background turbulence, $\varepsilon/(\varepsilon_{Wave} + B_0)$ are presented in Figure 7c. The normalized TKED values converge together from water surface to depth of z= 1.25 λ_w (Figure 7c), where the average of normalized TKED values is approximately one. This indicates that the wave-generated turbulence plays a dominant role on the near-surface TKED value in comparison to the surface convection and internal turbulence, and that is why the layer from the water surface to the depth of z= 1.25 λ_w is called the "wave-affected layer" in our paper.

2.4.4. Wave-generated TKED

The mean flow velocity increase resulted in the increment of the mean square slope (MSS) and wavelength λ_w (Table 1). The TKED has a larger value while the MSS increases (Figure 8c), and they have the same order of magnitude, i.e., MSS $\sim\varepsilon$ bellow the water surface z=0.005 m. The TKED for the different mean flow velocities were compared at three different depths (Figure 8d) to investigate the effects of the nonbreaking surface wave and the grid-generated turbulence on the TKED along the water column. Fig. 7d indicates that at a depth of z=0.145 m, the TKED change rate (red line) is higher than at z = 0.005 m (black line) while the surface heat flux was constant. The TKED comparison between the mean flow velocity range of 0.066 m/s to 0.183 m/s at the different depths shows that the TKED values increase ≈ 780 %, 370 % and 95 % at a depth of z=0.145 m, z=0.0175 m, and z=0.005 m, respectively (Figure 8d). By considering constant heat flux during the experiment, the TKED change rate should be the same by getting close to the water surface if the grid was the only source of turbulence. The different change rates, like wave scaling results (Figure 7c), indicate that the nonbreaking waves play a dominant role in the TKED on the

surface layer. The subtraction of the averaged-TKED within the wave-affected layer, $\varepsilon_{1.25\lambda_w}$, from the background TKED, ε_0, is considered the wave-generated TKED, $\varepsilon_{\text{wave-generated}} = \varepsilon_{1.25\lambda_w} - \varepsilon_0$. The wave-generated TKED for wavelength of 0.038 m $<\lambda_w<$ 0.098 m ranged to $4.9 \times 10^{-6} - 7 \times 10^{-6}$ m^2/s^3 (Figure 8e). Given that the breaking wave is often related to the enhanced TKED values within the surface layer, the $\varepsilon_{\text{wave-generated}}$ values represent the significant role of nonbreaking waves on the upper-ocean mixing intensity. It indicates well-documented researches are necessary to shed light on our poor understanding of the nonbreaking wave-generated turbulence. Also, it depicts that the precise values of nonbreaking wave-generated TKED are required to quantify the air-sea interface processes.

2.5. Conclusion and summary

Oceanic turbulence measurements are practically impossible when attempting to address processes taking place within few upper centimeters below wave ocean surface. The aim of our experiment was to investigate in a controlled laboratory setting how the of the horizontal heat and eddy fluxes affect the nearsurface layer.

In the experiment, the TKED ranges generated by the turbulence generating grid, $\varepsilon \approx 0.5\text{-}2.5 * 10^{-5} m^2/s^3$, at a distance of x/M=36 m where the surface boundary layer was investigated were the subset of the ocean TKED range, $\varepsilon \approx 10^{-11}$ - 10^{-3} m^2/s^3 (McMillan et al., 2016; Lozovasky et al., 2017, and Evan et al., 2018). The heated-grid generated a horizontal heat flux of 16.6 kw/m^2which is smaller than the Kuroshio front region, ~6.2 $*10^4$ kw/m^2 (Pan and Sum 2018) and the average net vertical heat flux of $Q \approx |25| w/m^2$in our experiment was not significant in comparison to the mean range of net vertical heat flux in the ocean $Q < |150| w/m^2$ (Carton

2018). The surface waves, with a wavelength range of $0.016\ \text{m} < \lambda_w < 0.066\ \text{m}$, were in the categorization of the capillary wave and the short gravity wave ranges (Munk 1951, and Chen et al., (2019).

While analyzing the vertical TKED variability, we have observed that there is a "wave-affected layer" from the water surface to a depth of z= 1.25 λ_w. The TKED associated with nonbreaking waves $\varepsilon_{\text{wave-generated}}$ ranged to $4.9 \times 10^{-6} - 7 \times 10^{-6}\ \text{m}^2/\text{s}^3$ for the wavelength range of 0.038 m $<\lambda_w<$ 0.098 m categorized as the gravity and gravity-capillary regimes (Munk et al., 195, Laxague et al., 2016, Chen et al., 2016). The increase of the MSS resulted in the larger TKED, and they have the same order of magnitude MSS ~ ε. Given that the nonbreaking waves typically cover a larger fraction of the ocean surface, 90–100 %, (Anguelova et al., 2006) than breaking waves, the TKED results indicate their significant contribution to the ocean energy budget. Therefore, the nonbreaking wave's TKED budget has to be considered to properly quantify the air-sea interface processes such as cool skin thickness (Alappattu et. al., 2017) which is a fundamental parameter required for quantifying the physical process taking place at the air-sea interface like the gas transfer (Fredriksson et. al., 2016) and heat transfer (Liu et. al., 2020)

We also found that the TD changes, which is the small-scale temperature fluctuation, are consistent with the large-scale temperature gradient, d<T>/dz, changes. The value of the THF is approximately constant within the surface layer. It represents that the measured THF near the water surface can be considered a surface water THF in the ocean, challenging to measure directly.

We also found that the power-law exponent of the tank is m=1.25 and m=1.13 for the decay of TD and temperature variance, respectively, and the decay of TKED equals 1.01<n<1.18 for the velocity range of 0.066 m/s < <U> < 0.183 m/s. From the observed results, we noticed that there were other sources that regionally amplify the temperature variance, TD, and TKED along the

tank, in addition to the grids. Based on that, the extra terms were added to the transport equation of temperature variance and mean turbulent kinetic energy.

The future work would be to connect the laboratory observation to the field observation. We will explore whether the THF value is constant within the upper ocean boundary layer as observed in this research. We would also like to study the importance of TKED below the nonbreaking gravity wave and investigate if the observed affected layer in this paper is common properties below the nonbreaking and breaking waves in the ocean.

Acknowledgments. We would like to thank RSMAS Ph. D. students: Sanchit Mehta, Hanjing Dai and Andrew W. Smith for help with the preparation of the experiment. This work was supported by the Gulf of Mexico Research Initiative grant and the National Science Foundation grant 1434670. The data are publicly available through the Gulf of Mexico Research Initiative Information and Data Cooperative (GRIIDC) at https://data.gulfresearchinitiative.org (doi: doi:10.7266/8P7590DJ).

CHAPTER 3: ASYMMETRIC FRONTAL RESPONSE ACROSS THE GULF OF MEXICO SUBMESOSCLAE FRONT IN WINTER 2016

3.1. Abstract

The interaction of cold Mississippi River water mass with the Gulf of Mexico in January 2016 resulted in a sharp front. The water on the Mississippi side was cold and vertically stratified (CVS) while the other side of the front the water was warmer and horizontally stratified (WHS). Here we investigate the horizontal and vertical variability of the turbulent kinetic energy dissipation rate (TKED), the temperature dissipation rate (TD), and the surface heat flux across a submesoscale front.

Our cross frontal observations demonstrated the presence of two distinct vertical layers with the first layer spanning depths 0-9 m while the second layer extends over depths 9-30 m.

The cross frontal deep layer (9-30 m) averaged TD varied by a factor 1000 and was larger on the CVS side. The near-surface layer averaged TD was similar across the front. The deep layer asymmetry coincides with the depths where the Thorpe displacement was large.

The situation was similar for layer averaged TKED.

Within the first and the second layer, the averaged TKED values were 10-30 times larger on the CVS side which was influenced by the cool Mississippi water when compared to the WHS side.

We posit that the TKED CVS-WHS asymmetry within the 9-30 m layer was due to the action of breaking internal waves as the enhanced TKED coincided with part of the water with larger values of the mean buoyancy frequency and large values of Thorpe displacement.

The reverse frontal asymmetry persisted in the surface turbulent heat fluxes. The WHS side was characterized by turbulent heat flux 4 times larger when compared to the CVS side. The frontal asymmetry was also imparted on the vertical transport of neutrally buoyant contaminants located at the surface to a depths of 14 m on the CVS side while staying surface-bound on the WHS side. This observation implies surface contaminants in the vicinity of CVS front side are likely to be dispersed over depths up to 14 m.

3.2. Introduction:

The lateral gradient of density and the gradients of temperature and salinity, with a boundary between two distinct water masses, make up oceanic fronts (Tintore et al., 1988 and Jaeger and Mahadevan 2018). Fronts are observed frequently across the global ocean where different water masses collide: the Gulf Stream (Xue and Mellor 1993 and O'Neill et al. 2017), the Agulhas Current (Ikehara et al. 2017; Hall et al. 2019), the Kuroshio Extension (Taguchi et al. 2009; Konda et al. 2010 and de Vries et al. 2019), and the northern part of the Gulf of Mexico (Luo et al. 2016 and Sun et al. 46 2020).

Fronts are important oceanic features that strengthen and modify the turbulent boundary layer (D'Asaro et al. 2011). The turbulence associated with mesoscale fronts (10-1000 km) and submesoscale front (0.1-10 km) have been observed modifying turbulent fluxes in heat (Liu et al. 2020) biogeochemical particles (Petrenko et al. 2017), and air-sea gas transfer (Baschek 2002).

For example observations of the front at the Kuroshio current indicated that the TKED within the frontal mixed layer is enhanced by up to two orders of magnitude (Nagai et al. 2009; D'Asaro et al. 2011)

Observations of the front at Kuroshio current by D'Asaro et al. (2011) indicated that the TKED within the frontal mixed layer is enhanced by one to two orders of magnitude. Nagai et al., (2009) have done direct observations on both sides of the Kuroshio front between 0.2-1.2 of the MLD (Mixed Layer Depth), contrary to D'Asaro et al. (2011) observations, they investigate TKED at the front without separating both sides from each other. Nagai et al., (2009) indicated that the TKED are an order of magnitude larger than predicted by wind scaling in the south of the front, while the D'Asaro et al. (2011) observed that the wind and surface cooling could not explain the high turbulence level at the front. The observations by Okey and Elliott (1977), and Inoue et al., (2010) found that large TKED values within the front can be attributed to internal wave (IW) breaking. However, the detailed mechanisms responsible for the enhanced value of TKED, turbulent fluxes, and mixing across the front remain unclear and need more detailed observations, especially within the upper mixed layer.

For this reason, the high-resolution microstructure measurements were used to address the turbulence variability on both sides of a submesoscale front from the water surface to 0.4 of the MLD. This paper aims to quantify horizontal and vertical TKED and TD variability across the front and their vertical transport effects. The paper is organized as follows: the field overview, the observation location, and instruments are introduced in sections 2.2-2.3, followed by the results and discussion sections 2.4-2.5. The conclusion is presented in section 2.6.

3.3. Overview of the Field Experiment

Data presented in this paper were collected during the LAgrangian Submesoscale ExpeRiment (LASER) in the northern part of the GOM during the winter of 2016 (Fig. 9). LASER was undertaken by

CARTHE (Consortium for Advanced Research on Transport of Hydrocarbons in the Environment) as a large scale study of oceanic surface lagrangian transport and dispersion. The R/V Walton Smith was used during LASER as a main mobile oceanographic and atmospheric sensor platform. As a part of the experiment, we have documented the presence of a submesoscale front generated by the interaction of cold Mississippi river water with continental shelf water, which may be affected by the warm loop current generated in the GOM (Jouanno et al., 2016; Shao et al., 2019; Bogucki et al., 2020). The numerical simulation suggested that the interaction of the Mississippi river water with loop current eddies is the primary driver of the front (Luo et al., 2016). Luo et al., (2016) also argued that the fronts are generated primarily by frontogenesis and mixed layer instabilities in winter, while in summer, the frontogenesis fueled by the horizontal density gradients generated by the river is the dominant driver. A detailed overview of frontal dynamics during LASER are in McWilliams (2016), D'Asaro et al., (2018), Barken et al., (2019), and D'Asaro et al., (2020).

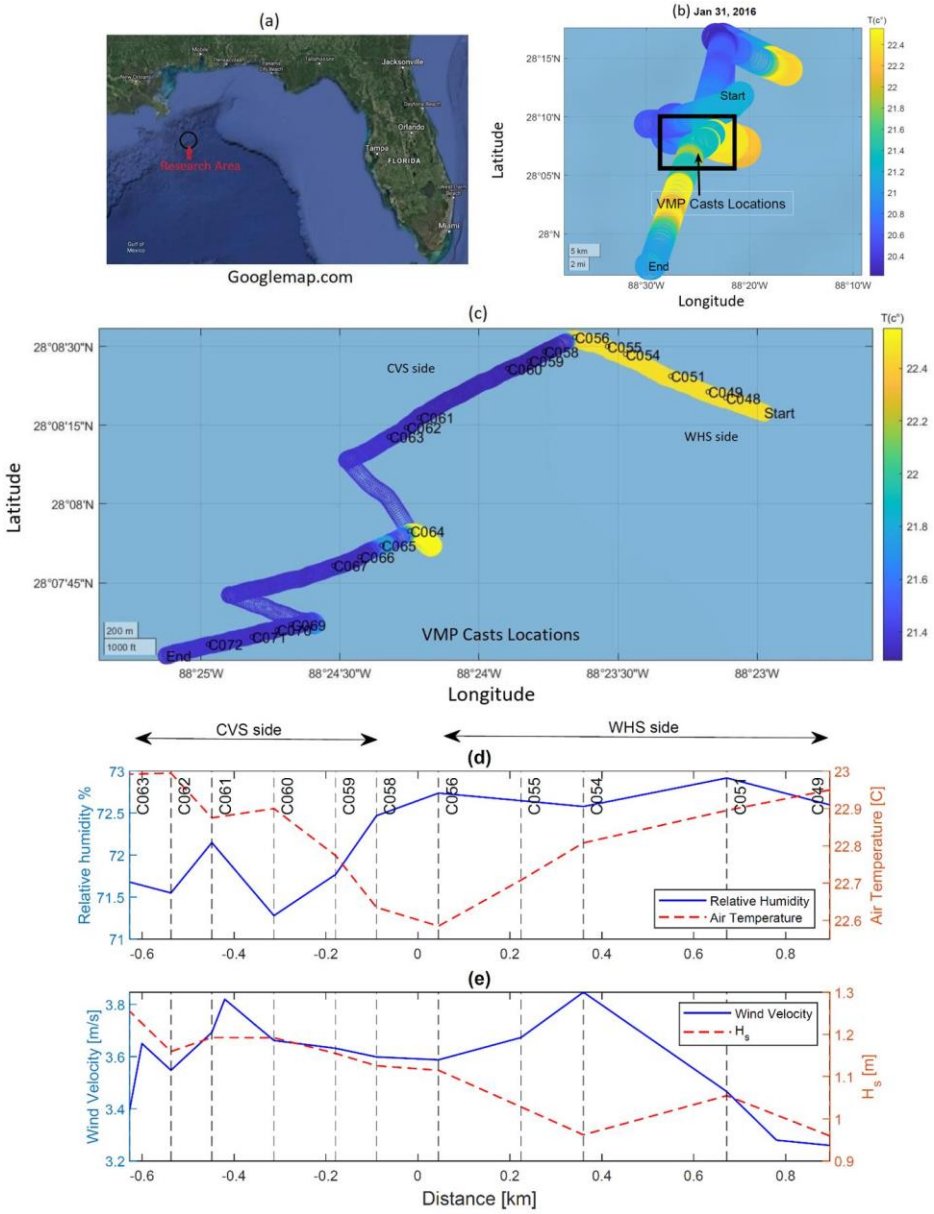

Fig. 9 (a) The location of data collection in the northern part of the GOM. (b) The surface temperature colors the ship track. (c) The subdomain of the ship track where the VMP200 collected the vertical profiles of ocean properties is shown. (d) The relative humidity, (d) the air temperature, (e) the wind velocity, and (e) significant wave height, H_s, are presented across the front. The vertical dashed-lines in graphs d-e give the horizontal distance of the VMP200 deployments for upcasts C049 to C063 from the front center shown by zero distance.

3.4. Experimental methods

The University of Miami research vessel, R/V Walton Smith, provides a stable platform for oceanic turbulence, hydrographic, and air-sea flux sampling. During LASER, the vessel passed over the front (Fig. 9). The hydrographic and atmospheric data collected by the ship are presented in Figs. 9d-e and includes the relative humidity, air temperature, wind velocity, and significant wave height (H_s). The water surface elevation was observed by the ultrasonic distance meter (UDMS, Senix ToughSonic). The ship's motion and rotation were measured using linear accelerometers (Columbia Research Model AS-307 HPTX) and rotation rate gyros (SYSTRON Donner QRS11-00050-630), respectively. The method of Drennan et al., (1994) was used to calculate the actual surface wave height. In this method, the displacement of the wave created by ship motion and rotation was corrected. The ultrasonic anemometer (RM Young 81000) was mounted at 4.6 m above the water surface to measure the wind speed, and a Campbell Scientific IRGASON was mounted at 5.36 m above the water surface to measure the relative humidity and air temperature.

The surface roughness was measured by a Helmholtz-Zentrum Geesthacht Marine X-band Radar (MR) mounted on top of the wheelhouse covering a 360 degree azimuthal range. The hydrographic data collection method is described in detail at Shao er al. (2019) work. We present results from 13 of the approximately 97 vertical turbulence profiles across the mesoscale front. The turbulence data were collected with the aid of the Rockland Scientific vertical microstructure profiler (VMP200) (Lueck et al. 2002) for three days (from January 29 to January 31, 2016). The VMP200 was equipped with two orthogonally oriented shear sensors. Each shear sensor sampled the small-scale shear component orthogonal to the vertical axis with a 512 Hz sampling rate. The VMP200

was also equipped with a fast thermistor (model FP07, 7 ms response time, and sampled at 512 Hz) and fast conductivity sensor (Sea-Bird SBE7 response time less than 1 ms, sampled at 512 Hz).

The VMP200 was deployed in two modes: free-falling and free-uprising. In the free-falling mode or the downcast mode, the VMP200 is negatively buoyant. In this mode, while deployed from the ship's deck, the VMP200 was permitted to free fall to a depth ≈110 m which was beneath the seasonal mixed layer depth. In free-falling mode, we only report data only from the depths z>5m to avoid the contamination of TKED and TD near-surface data by the ship wake (Luecket al. 2002). The terminal velocity of the VMP200 while in free fall was around 0.72 m/s.

To sample the near-surface part of the water column, we used the VMP200 in a ’free uprising' mode or the upcast mode (Lueck et al. 2002). The VMP200 system included a buoyancy collar, to make is positively buoyant, and a remote-controlled weight release mechanism. The release of the weight - freed the VMP200 to start freely rising towards the surface. The presented here data were collected when the uprising VMP200 attained its terminal velocity of 0.65 m/s.

The methodology of free rising deployment was as follows: we first lowered the instrument to a predetermined depth, typically around 40 m below surface. While the ship was in a slow wind-induced drift we then waited until the ship left the area where the VMP200 would likely emerge. Once the ship was relatively far away from the VMP200 then we released the weight, freeing the VMP200 to start its rise towards the surface. This approach permitted us to sample the near-surface in more detail while the VMP200 was traveling vertically with its terminal velocity.

The upcast deployments that were recovered close to the ship (<100 m) were eliminated. The VMP200 data were processed using the standard approach (detailed by Lueck et al. (2002)) and we converted temporal shear gradients to corresponding spatial gradients assuming by invoking

Taylor's frozen field hypothesis (Lueck et al. 2002). The profiles presented here were characterized by the VMP200 shear sensor attack angle <10 deg. All presented data were quality controlled for factors affecting the TKED data quality such as attack angle, spikes (Lueck et al. 2002).

Following the standard assumption that the oceanic flow can be approximated by idealized homogenous and isotropic turbulence (Lueck et al. 2002) the TKED (or ε) can be derived from the VMP200 measured shear spectrum ψ(K) as (Lueck et al. 2002):$\varepsilon \approx \frac{15}{2} \nu \int_0^{\infty} \psi(K) dK$, where k is the wavenumber, and ν is the kinematic viscosity. The rate of temperature dissipation TD (or χ) can be obtained from the VMP measured one dimensional temperature gradient spectra, $\phi(k)$, as (Bluteau et al. 2017): $\chi \approx 6 K_{\theta} \int_0^{\infty} \Phi(K) dK$, where K_{θ} is the thermal molecular diffusivity. The FP07 thermistor used in VMP200 does not fully resolve the temperature variance of the underlying temperature field when (Lueck 1977) traveling through the water column faster than 0.1 m/s. In our measurements presented here, the terminal VMP200 rising speed was ≈ 0.65 m/s. The VMP measured vertical TD profiles thus represent underestimates of the 'real' the water column TD, as we did not correct the TD by the FP07 spectral response function (Lueck et al. 1977) (Fig. 10b). The VMP200 upcasts method permitted very accurate observations of the near-surface layer as the VMP200 rise was constant at 0.65 m/s till it reached the surface with the vertical bin resolution of ≈1 mm for salinity and temperature and ≈ 0.5 m for TD, and TKED data. The VMP200 consecutive casts denoted as C048 to C072 are presented in Fig. 9. The upcasts C048 to C056 were collected on the WHS front side while the casts C058 to C072 were acquired on the CVS side. The center of the front was assumed to be the center of the region where the sea surface temperature changed by 1.5 ℃ over 5 km (Shao et al. 2019). The precise front location was estimated from the surface roughness variability measured by ship-based marine radar (Shao et al. 2019)) and coincided with

the VMP200 cast C064. The downcast profiles, C071 and C072, were carried out to the depth around 110 m and traversed the full extent of the mixed layer (Fig.11).

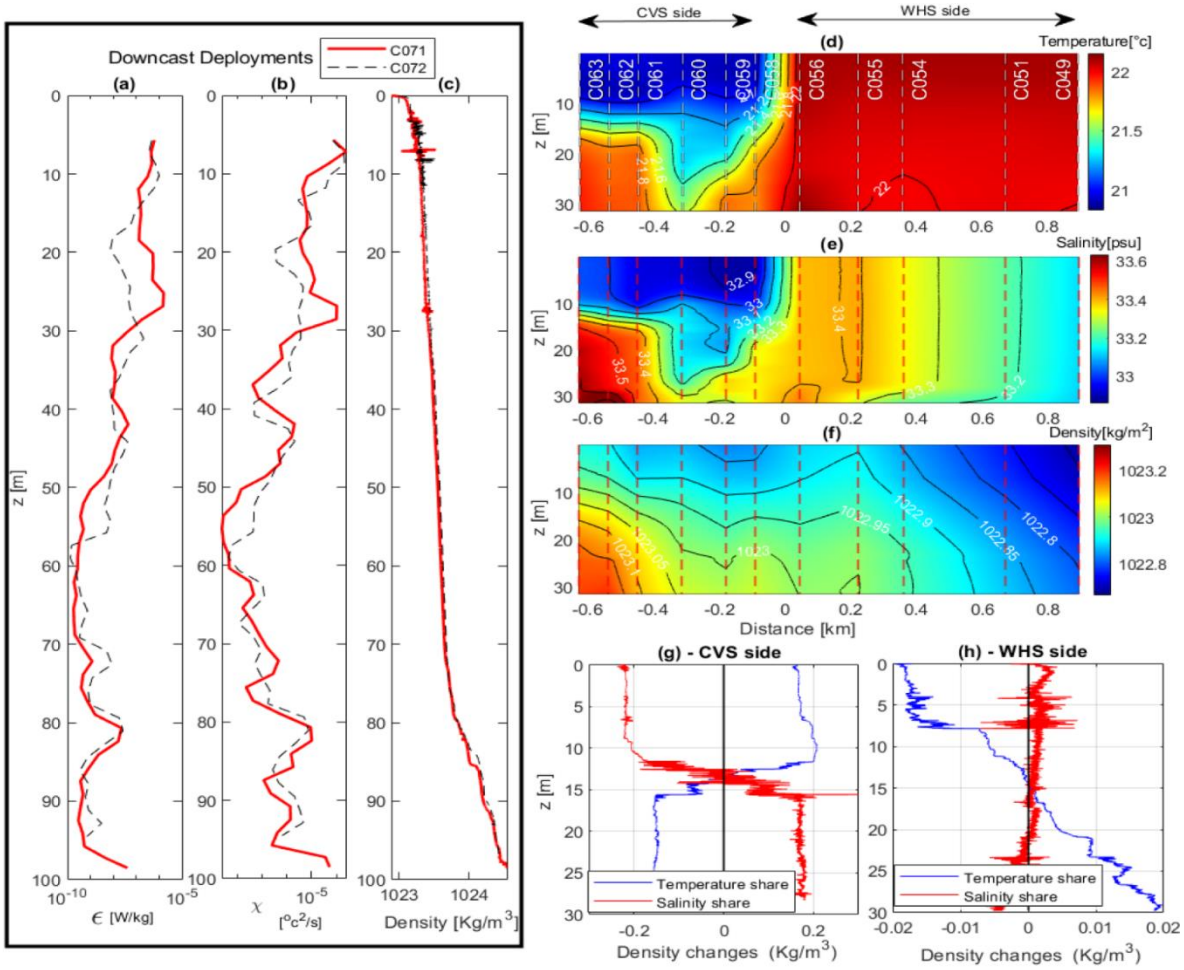

Fig. 10 The vertical profiles of the VMP200 deployments on the CVS side are shown in a black box for downcasts C071 and C072. (a) TKED, (b) TD, (c) water density. VMP200 derived transects of the front when the instrument was deployed using the upcast technique are shown in graphs (d) Temperature, (e) salinity, and (f) density. The vertical dashed lines present the location of deployments, and the zero distance shows the location of the front center. The relative contribution of salinity and temperature to density are shown on (g) the CVS (C060) and (f) WHS (C054) sides.

3.5. Results

The air-side data collected during the front transect are presented in Figs. 9d-e. The relative humidity on the WHS side (relative humidity is 72.65 %) was on average 0.5 % higher than CVS side (relative humidity is 72.30 % (Fig. 9d). On the CVS side, the air temperature dropped from ≈22.90 ℃, at C049, to ≈22.70 ℃, at C055 while on the WHS side, the air temperature was increased with distance from the front center, and reached to ≈23 ℃, at C063. The average air temperature was approximately the same on both sides of the front (Fig. 9d).

The dominant wind direction was across the front from the WHS side to the CVS side. The wind velocity increased from ≈3.25 m/s, at C048, to ≈3.67 m/s, at C060, then it decreased to ≈3.25 m/s, at C063 (Fig. 9e). The average significant wave height, H_s, on the CVS side (H_s= 1.20 m) was ≈15 % larger than the WHS side (H_s = 1.05 m) (Fid. 1e). In Figs. 9-12, the vertical dashed lines present the location of the VMP200 deployments. The distance '0' coincides with the front center.

3.5.1. Mixed layer depth-the VMP200 downcast

The VMP downcast technique was used to study the ocean water column through the mixed layer depth (MLD). The downcast profiles of C071 and C072 were shown in Figs. 10a-c. The measured TKED and TD values decreased by about three orders of magnitude from z= 5 m to a depth of z=55 m. TKED and TD attained their maximum values of $\varepsilon \approx 1.45 * 10^{-6}$ w/kg (Nagai et al., (2009) observed $\varepsilon \approx 10^{-8}$-$10^{-6}$ w/kg in the Kuroshio front) and $\chi \approx 2 * 10^{-4}$ ℃ /s, within the depth interval ≈8 m to 10 m. The density profile (Fig. 10c) showed a large density variance over

depths from 3 m to around 9 m. The observed seasonal mixed layer depth was found to be around 80 m when using the criteria (de Boyer et al., 2004) corresponding to the change of density $\Delta\rho$= 0.03 kg/m^3over a 10 m depth.

3.5.2. Salinity, temperature, density the vertical and horizontal variability obtained from the VMP200 upcasts

A more detailed picture of the front structure can be gleaned from the VMP200 series of vertical upcasts C049-C063, collected between 18:40 to 20:10 UTC. The horizontal resolution of the surface data are approximately 150 m. In Figs. 10d-f, we present the front cross-section of the salinity (S), temperature (T), and density (ρ) as a function of depth and horizontal distance from the front center. At the surface, the water properties such as T or S changed rapidly over a 200 m distance, which corresponds to an approximate front width (Figs. 10d-e). The cold front side, CVS, consisted of a vertically stratified water colum (Fig. 10f). The warm front side, WHS, was characterized by a set of tilted density layers (Fig. 10f) with a strong horizontal salinity gradient and relatively weak vertical salinity variability (Fig. 10e).

To compare the relative contribution of the S and T to density across the front, we plotted their relative contribution to density (McDougall et al. 2003) using two selected VMP200 profiles, each from either CVS or WHS side of the front (Figs. 10g and 10h). The CVS side was characterized by large and compensated T and S contribution to density when compared to the WHS side. On the WHS side, the S contribution to density was weaker with the temperature dominating the density variability. Each T and S vertical contribution to density, had its contribution sign changed at around 15m depth (Figs. 10g and 10h).

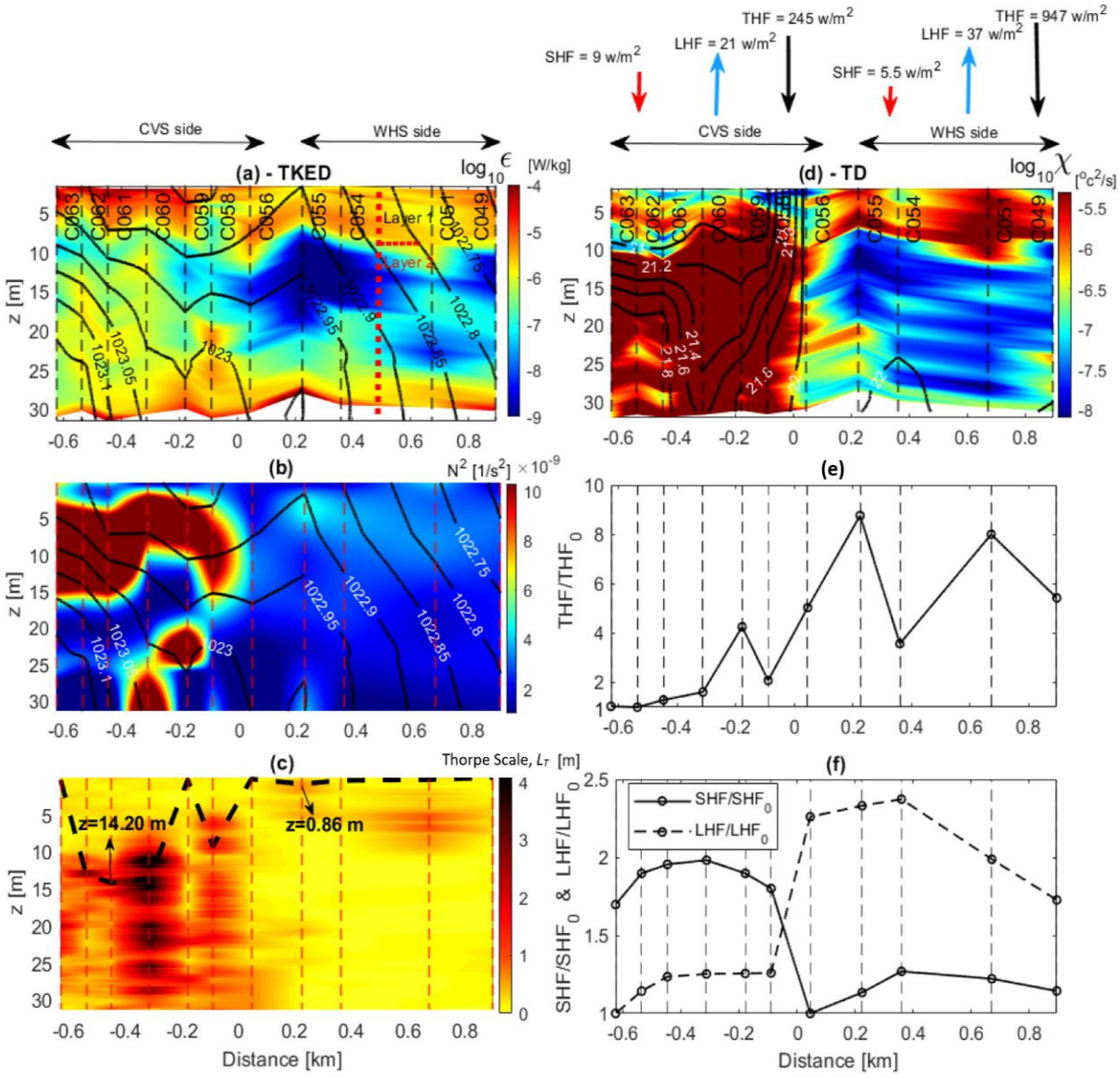

Fig. 11 (a) The TKED vertical profiles across the front. The red-dashed line separates the two observed layers of TKED. (b) The buoyancy frequency square, N^2 is shown. The black contour lines in (a-b) are shown the density. (c) The one meter-mean of the Thorpe sca, L_T. The black-dashed line presents the maximum depth that the water parcel can reach the water surface due to the vertical overturning. (d) The TD vertical profiles. The black counter lines of temperature are depicted. The direction and the average value of the surface SHF, LHF, and THF are presented on

both sides of the front by arrows (the arrows are not scaled). (e) The THFs of every upcast divided by its minimum value, THF_0, is shown. (f) The SHF and LHF at the water surface divided by their minimum values named as SHF_0 and LHF_0, respectively, are shown. The vertical dashed-lines in graphs (a-f) present the location of the VMP200 deployments at different distances from the front center, shown by zero distance.

3.5.3. Cross frontal TKED vertical and horizontal variability

The horizontal and vertical variability of the TKED inferred from uprising VMP200 profiles are in Fig. 11a. As argued earlier, the TKED within the upper 5 m layer and possibly up to 9 m, Fig. 13a, and across the front was enhanced by the action of surface waves. The CVS front side was characterized by a large value of the buoyancy frequency feature a 'tongue' (5-15m depth), Fig. 11b, and a relatively unstratified water column on the WHS side.

The VMP200 high-resolution density measurements permitted to measu Thorpe scale, $L_T = <L^2>^{1/2}$ (Bogucki et al., 2020 and Jackson et al., 2008), map (Fig. 11c), where L is Thorpe displacement. The estimated accuracy of the L, found from their distribution, was around 0.2 m. Thorpe displacement is the water particle displacement needed to move the observed water particle from its current depth to form a stable density profile. That obtained displacement applies mostly to the shear-driven turbulence (Smith et al., 2020 and Jackson et al., 2008).

The Thorpe scale map (Fig. 11c) shows large cross frontal asymmetry with the largest L_T values on the CVS side. The CVS side is more likely to disperse surface neutrally buoyant contaminants down to 14.2 m at the -0.4 km distance from the front center (the black-dashed line in Fig. 11c).

Thus when considering the oil spill as a surface neutrally buoyant contaminant (Fingas et al., 2006), the surface-bound oil will more likely be vertically dispersed on the CVS side.

3.5.4. Turbulent heat flux TD variability along the front

Based on the VMP data, we estimated the vertical turbulent heat flux (THF) defined (Moum 1996) as $\mathrm{THF} = -\frac{1}{2}\rho C_p \chi / T_z$, where the $C_p$is the specific heat of the water and the T_z is the temperature gradient. The surface is defined here as a part of the water column where the mean T_z and the TD were measured by the VMP200 upcasts and represent depth average from the actual sea surface to depth 0.15 m and 0.5 m for T_z and TD, respectively. Based on air-side measured parameters, Fig. 9d-9e, we have calculated the values of the sensible heat flux (SHF), and the latent heat flux (LHF) at the water surface (Edson et al. 2013).

The averaged value of the surface heat fluxes and its direction for both side of the front combined with the TD cross-front map is presented in Fig. 11d. The TD graph presented two layers on each side of the front (Fig. 11d) same as TKED graph (Fig. 11a). The first layer started from the water surface to a depth $z \approx 9$ m, and the second layer was created below a depth $z \approx 9$ m.

The measured horizontal asymmetry across the front of the surface THF, normalized to its lowest value, is presented in Fig. 11e. The WHS side exhibited surface THF larger by a factor of 4 than the CVS side, a striking anomaly and likely contributing to enhanced air side heat fluxes. The large values of the THF were mostly driven by the weaker near-surface mean temperature gradient and hence were larger on the weakly stratified WHS side (Fig. 10f).

The rest of the heat fluxes (SHF/LHF) vary only by a factor of 2 when crossing the front (Fig. 11f).

The air temperature was larger than the water temperature, and the air-water temperature difference was $\Delta T \approx$ 0.41 ℃ and $\Delta T \approx$ 1.56 ℃ on the WHS and CVS sides, respectively. The small temperature difference resulted in a small SHF of ≈9 w/m^2, positive value means that the heat inserted to the ocean, for the WHS side and ≈5.5 w/m^2 for the CVS side (Figs. 11 d and 11f). The larger LHF ≈-37 w/m^{2}on WHS side in comparison to the CVS side, LHF ≈-21 w/m^2 (Figs. 11 d and 11f) was due to the larger relative humidity (Fig. 9d) on the WHS side .

3.6. Discussion

3.6.1. The wave effects on the vertical TKED distribution

The atmosphere properties of relative humidity, air temperature, wind velocity, significant wave height, Fig. 9d and 9e, and the solar insolation (not shown here) were relatively constant. The average significant wave height,H_s, on the CVS side was H_s= 1.20 m and H_s= 1.02 m at the WHS side (Fig. 9e). The vertical profiles of the TKED are presented in Fig. 12a. To assess surface wave's effect on the vertical TKED profiles on either side of the front, we have compared measured TKED profiles to predicted vertical TKED $\varepsilon_{AM}(z)$ due to the action of surface waves (Esters et al. (2018) and Anis and Moum (1995)).

In general the surface waves were observed (Anis and Moum 1995; Esters et al. 2018) to follow the depth dependent TKED as:

$$\varepsilon_{AM}(z) = 2K\alpha_1 u_{s0} {u_*}^2 * e^{-2Kz} \quad (5)$$

Here u_{s0} is the wave Stoke drift at the ocean surface, and α_1 is a dimensionless constant associated with the surface waves, $\alpha_1 = 3.75b\pi\sqrt{H_s/\lambda}$. Λ is a dominant wave wavelength. b is an empirical constant ranging between 0 and 1, and u_* is friction velocity. $u_* = \sqrt{\tau/\rho}$, where τ is wind stress and ρ is seawater density.

The vertical TKED profiles normalized by $\varepsilon_{AM}(z)$ presents converging of the data from a depth of 5 m up to the water surface and approximately 6 times larger than inferred from Eq. (5) (Fig. 12a). The normalized TKED with $\varepsilon_{AM}(z)$ had a better estimation than the wind scaling $\varepsilon_w(z) = {u_*}^3/kz$ (Esters et al., 2018), where k is von Karman constant, and the surface buoyancy flux B_0 (Zahariev et al., 1997) due to that the normalized ratio of $\varepsilon/\varepsilon_{AM}(z) \approx 6$ is smaller than $\varepsilon/\varepsilon_w(z) \approx 180$ and $\varepsilon/B_0 \approx 130$ over the depth 0-5 m (Figs. 12b-c). Given that the wave-generated turbulence predicts the TKED values better than other methods, it indicates the role of the surface wave on the TKED values compared to the other sources of surface turbulence.

We attribute the observed normalized TKED value departure from 1, over 0-5 m depth, to the limitation of Equation (6) where the waves were characterized by a single parameter, dominant wave height, and wavelength. The reality of the oceanic wave field is more complex since the upper few meters are likely dominated by shorter wind waves, while at depth the dominant effect is the longer wavelength swell (Anis and Moum 1995). We then thus posit that the upper 5 m represents wave affected portion of the underlying mixed layer.

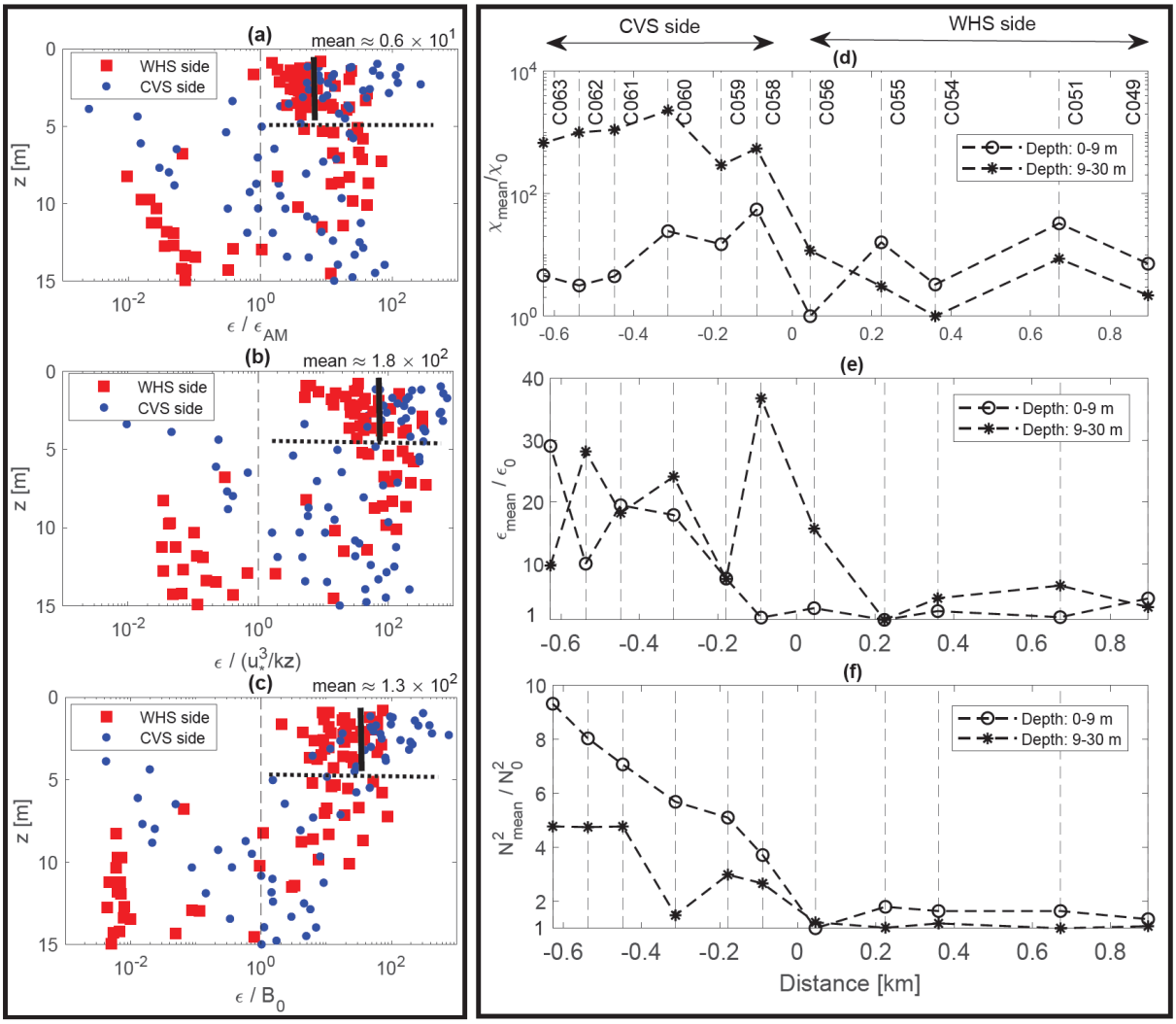

Fig. 12 (a) The normalized TKED values with wave slaing (Anis et al., 1995), Eq.1, (b) wind scaling, $\varepsilon_w\,(z) = u_*^{\,3}/kz$, (c) and surface buoyancy flux scaling, B_0, methods. The horizontal dashed and vertical solid black lines in (a) to (c) present the depth of converging data and the average value of the normalized TKED, respectively. The averaged water column properties across the front at two different depth ranges of z=0-9 m and z=9-30 m are presented in (d) to (f). (d) The averaged water column of TD, χ_{mean}, divided by the minimum averaged value of TD for that layer, χ_0, is shown. (e) The averaged TKED, ε_{mean}, and (f) the averaged buoyancy frequency

square, N^2_{mean}, normalized by their minimum averaged value for that layer showing by ε_0 and N^2_0, respectively, are presented. The vertical dashed-lines in graphs (d-f) present the location of the VMP200 deployments at different distances from the front center, shown by zero distance.

3.6.2. Layer averaged properties across the front

Now we are in a position to analyze layer averaged properties across the front. We have divided the water column into two distinct layers: the near-surface layer or first layer, affected by surface waves, and extending from z=0 to 5 m (Fig. 12a) and possibly up to 9 m depth (Fig. 11a). The second layer, the mixed layer interior, includes the water column extending from z=9 to 30 m. Within each layer, the average of the water column properties such as TD, TKED, and buoyancy frequency square, N^2 are normalized by their minimum value for that layer (Figs. 12d-f)

The surface layer (0-9 m depth) averaged TD normalized to their lowest layer averaged value is roughly symmetrical around the front center (Fig. 12d). The averaged and normalized TDs for the deeper layer (9-30 m depth) show strong TD cross frontal asymmetry with the TD values on the CVS side larger by a factor of 1000 than on the WHS side.

The CVS side presented 10 to 30 times larger TKED than the WHS side and irrespective of the layer depth (Fig. 12e). The normalized N^2 (Fig. 12f) was larger on the CVS side by a factor of 5-10 when compared to the WHS side. The near-surface (averaged within 0-9 m depth) N^2 was the largest on the CVS side, as it likely reflects the effects of the near-surface stratification on that side.

We hypothesize that the internal wave (IW) breaking enhanced the TKED values on the second layer of the CVS side based on (Oakey et al., 1997), and (Inoue et al., 2010) observations. They found that the large TKED values within the front can be attributed to the IW breaking. A modeled IW dissipation, ε_{GH}, calculated based on Gargett et al., (1984) work, is used as an estimate of IW related TKED. The model contains a simple parametrization of the IWs generated TKED and assumes a constant value of the IWs energy density, E_d. Following that assumption, the ε_{GH} yields the IW field TKED as $\varepsilon_{GH} \approx E_d N$ (Gargett et al., 1984). The ratio $\varepsilon_{GH}/\varepsilon_{mean}$ is vanishingly small in the upper 9 m. It attains a value of $\varepsilon_{GH}/\varepsilon_{mean}$=0.1 on the CVS side within 9-30 m depth interval, in other words, 10 % of the measured TKED can be contributed to the IW breaking. It indicates that the IW presence may be a correct hypothesis; however, there is no further proof in this paper. More detailed research is considered necessary to prove the hypothesis.

3.7. Conclusion

The observed frontal pattern in the world's largest marine ecosystem (Belkin et al., 2007) indicates the importance of fronts in oceanic circulation and their role in the oceanic surface layer dynamics. Hence, this paper addresses turbulence variability across a submesoscale front in the GOM in the winter of 2016. The cross-section of the front revealed large horizontal variability of the surface heat flux, TD, and the ability of surface turbulent processes to remove neutrally buoyant surface-bound contaminants.

We observed large surface THF frontal asymmetry with the WHS side exhibiting up to 4 times larger surface THF. The rest of the heat fluxes (SHF/LHF) varied by only a factor of 2 when

crossing the front. This asymmetry was likely reflected in the cross-front variability of atmospheric dynamics.

The cross-frontal observations demonstrated two vertical layers with the first layer spanning depths 0-9 m while the second layer extends over 9-30 m. The cross frontal deep layer (9-30 m) averaged TD varied by a factor of 1000 and was larger on the CVS side. The near-surface layer (0-9 m) averaged TD was similar across the front. Within the deep and near-surface layers, the averaged TKED values were 10-30 times larger on the CVS side which was influenced by the cool Mississippi water when compared to the WHS side. By measuring the Thorpe displacement, we posit that the CVS side surface-bound naturally buoyant particles were likely to experience eddies capable of submerging them up to 14.2 m depth with no such processes on the WHS side. The higher TKED on the vertical stratification side (or CVS side) has implications on the air-sea gas fluxes velocity, $K_g \sim \varepsilon^{1/4}$ (Fredriksson et al., 2016) and it is essential for the oil industry (Loh et al., 2020) due to that the higher turbulence enhances the biodegradation of oil (Ramirez et al., 2018). As fronts are common over the global ocean, the observed asymmetric response of the turbulence and their considerable variations across the front should be considered in the ocean-atmosphere climate system. The inaccurate boundary layer could cause substantial climate prediction error. Future research should involve investigating if our observations are common in other oceanic fronts.

Acknowledgments. This research was made possible in part by a grant from The Gulf of Mexico Research Initiative and in part by and the National Science Foundation grant 1434670. Thanks are given to all those who helped during the LASER experiment, in particular, the crew of the R/V 'Walton Smith'. We would like to thank Justin Trull for his help with the creation of the MATLAB

plots. Data are publicly available through the Gulf of Mexico Research Initiative Information and Data Cooperative (GRIIDC) at https://data.gulfresearchinitiative.org (DOI:10.7266/n7-y7gw-vy06).

REFERENCES

1. Anis, A. and Moum, J.N., 1995. Surface wave–turbulence interactions. scaling ε (z) near the sea surface. Journal of Physical Oceanography, 25(9), pp.2025-2045.
2. Agrawal, Y.C., Terray, E.A., Donelan, M.A., Hwang, P.A., Williams III, A.J., Drennan, W.M., Kahma, K.K. and Krtaigorodskii, S.A., 1992. Enhanced dissipation of kinetic energy beneath surface waves. Nature, 359(6392), p.219.
3. Antonia, R.A., Zhou, T. and Zhu, Y., 1998. Three-component vorticity measurements in a turbulent grid flow. Journal of Fluid Mechanics, 374, pp.29-57.
4. Babanin, A.V., 2006. On a wave-induced turbulence and a wave-mixed upper ocean layer. Geophysical Research Letters, 33(20).
5. Babanin, A.V. and Haus, B.K., 2009. On the existence of water turbulence induced by nonbreaking surface waves. Journal of Physical Oceanography, 39(10), pp.2675-2679.
6. Barkan, R., McWilliams, J.C., Shchepetkin, A.F., Molemaker, M.J., Renault, L., Bracco, A. and Choi, J., 2017. Submesoscale dynamics in the northern Gulf of Mexico. Part I: Regional and seasonal characterization and the role of river outflow. Journal of Physical Oceanography, 47(9), pp.2325-2346.
7. Barkan, R., Molemaker, M.J., Srinivasan, K., McWilliams, J.C. and D'Asaro, E.A., 2019. The role of horizontal divergence in submesoscale frontogenesis. Journal of Physical Oceanography, 49(6), pp.1593-1618.
8. Baschek, B., 2002. Air-sea gas exchange in tidal fronts (Doctoral dissertation).
9. Batchelor, G.K. and Townsend, A.A., 1948. Decay of isotropic turbulence in the initial period. Proceedings of the Royal Society of London. Series A. Mathematical and Physical Sciences, 193(1035), pp.539-558.
10. Batchelor, G.K. and Townsend, A.A., 1947. Decay of vorticity in isotropic turbulence. Proceedings of the Royal Society of London. Series A. Mathematical and Physical Sciences, 190(1023), pp.534-550.
11. Bluteau, C.E., Lueck, R.G., Ivey, G.N., Jones, N.L., Book, J.W. and Rice, A.E., 2017. Determining mixing rates from concurrent temperature and velocity measurements. Journal of Atmospheric and Oceanic Technology, 34(10), pp.2283-2293.

12. Bogucki, D.J. and Domaradzki, J.A., 2015. Temperature gradient spectra and temperature dissipation rate in a turbulent convective flow. Journal of Turbulence, 16(12), pp.1179-1198.
13. Bogucki, D.J., Huguenard, K., Haus, B.K., Özgökmen, T.M., Reniers, A.J.H.M. and Laxague, N.J.M., 2015. Scaling laws for the upper ocean temperature dissipation rate. Geophysical Research Letters, 42(3), pp.839-846.
14. Bye, J.A., 1965. Wind-driven circulation in unstratified lakes. Limnology and Oceanography, 10(3), pp.451-458.
15. Cant, R.S., 2001. SB Pope, Turbulent Flows, Cambridge University Press, Cambridge, UK. Combustion and Flame, 125, pp.1361-1362.
16. Collins III, C.O., Blomquist, B., Persson, O., Lund, B., Rogers, W.E., Thomson, J., Wang, D., Smith, M., Doble, M., Wadhams, P. and Kohout, A., 2017. Doppler correction of wave frequency spectra measured by underway vessels. Journal of Atmospheric and Oceanic Technology, 34(2), pp.429-436.
17. Comte-Bellot, G. and Corrsin, S., 1966. The use of a contraction to improve the isotropy of grid-generated turbulence. Journal of fluid mechanics, 25(4), pp.657-682.
18. D'Asaro, E., Lee, C., Rainville, L., Harcourt, R. and Thomas, L., 2011. Enhanced turbulence and energy dissipation at ocean fronts. science, 332(6027), pp.318-322.
19. D'Asaro, E.A., Shcherbina, A.Y., Klymak, J.M., Molemaker, J., Novelli, G., Guigand, C.M., Haza, A.C., Haus, B.K., Ryan, E.H., Jacobs, G.A. and Huntley, H.S., 2018. Ocean convergence and the dispersion of flotsam. Proceedings of the National Academy of Sciences, 115(6), pp.1162-1167.
20. D'Asaro, E.A., Carlson, D.F., Chamecki, M., Harcourt, R.R., Haus, B.K., Fox-Kemper, B., Molemaker, M.J., Poje, A.C. and Yang, D., 2020. Advances in Observing and Understanding Small-Scale Open Ocean Circulation During the Gulf of Mexico Research Initiative Era. Frontiers in Marine Science.
21. de Boyer Montégut, C., Madec, G., Fischer, A.S., Lazar, A. and Iudicone, D., 2004. Mixed layer depth over the global ocean: An examination of profile data and a profile-based climatology. Journal of Geophysical Research: Oceans, 109(C12).
22. de Vries, H., Scher, S., Haarsma, R., Drijfhout, S. and van Delden, A., 2019. How Gulf-Stream SST-fronts influence Atlantic winter storms. Climate Dynamics, 52(9-10), pp.5899-5909.

23. Djenidi, L., Kamruzzaman, M. and Antonia, R.A., 2015. Power-law exponent in the transition period of decay in grid turbulence. Journal of Fluid Mechanics, 779, pp.544-555.
24. Djenidi, L. and Antonia, R.A., 2014. Transport equation for the mean turbulent energy dissipation rate in low-$ R_ {\lambda} $ grid turbulence. Journal of Fluid Mechanics, 747, pp.288-315.
25. Donelan, M.A. and Plant, W.J., 2009. A threshold for wind-wave growth. Journal of Geophysical Research: Oceans, 114(C7).
26. Dourado, M. and Oliveira, A.P.D., 2001. Observational description of the atmospheric and oceanic boundary layers over the Atlantic Ocean. Revisita Brasileira de Oceanografia, 49(1-2), pp.49-59.
27. Drennan, W.M., Donelan, M.A., Madsen, N., Katsaros, K.B., Terray, E.A. and Flagg, C.N., 1994. Directional wave spectra from a Swath ship at sea. Journal of Atmospheric and Oceanic Technology, 11(4), pp.1109-1116.
28. Edson, J.B., Jampana, V., Weller, R.A., Bigorre, S.P., Plueddemann, A.J., Fairall, C.W., Miller, S.D., Mahrt, L., Vickers, D. and Hersbach, H., 2014. On the exchange of momentum over the open ocean. Journal of Physical Oceanography, 44(9), p.1589.
29. Elfouhaily, T., Chapron, B., Katsaros, K. and Vandemark, D., 1997. A unified directional spectrum for long and short wind-driven waves. Journal of Geophysical Research: Oceans, 102(C7), pp.15781-15796.
30. Esters, L., Breivik, Ø., Landwehr, S., ten Doeschate, A., Sutherland, G., Christensen, K.H., Bidlot, J.R. and Ward, B., 2018. Turbulence scaling comparisons in the ocean surface boundary layer. Journal of Geophysical Research: Oceans, 123(3), pp.2172-2191.
31. Fingas, M., Hollebone, B. and Fieldhouse, B., 2006, July. The density behaviour of heavy oils in water. In Proceedings of the twenty-ninth AMOP Technical Seminar (pp. 57-77).
32. Fredriksson, S.T., Arneborg, L., Nilsson, H., Zhang, Q. and Handler, R.A., 2016. An evaluation of gas transfer velocity parameterizations during natural convection using DNS. Journal of Geophysical Research: Oceans, 121(2), pp.1400-1423.
33. Funk, C.J., 1973. Multiple scattering calculations of light propagation in ocean water. Applied optics, 12(2), pp.301-313.

34. Garbe, C.S., Rutgersson, A., Boutin, J., De Leeuw, G., Delille, B., Fairall, C.W., Gruber, N., Hare, J., Ho, D.T., Johnson, M.T. and Nightingale, P.D., 2014. Transfer across the air-sea interface. In Ocean-Atmosphere Interactions of Gases and Particles (pp. 55-112). Springer, Berlin, Heidelberg.
35. Gargett, A.E. and Holloway, G., 1984. Dissipation and diffusion by internal wave breaking. Journal of Marine Research, 42(1), pp.15-27.
36. Gargett, A.E., 1989. Ocean turbulence. Annual Review of Fluid Mechanics, 21(1), pp.419-451.
37. Gargett, A.E. and Moum, J.N., 1995. Mixing efficiencies in turbulent tidal fronts: Results from direct and indirect measurements of density flux. Journal of Physical Oceanography, 25(11), pp.2583-2608.
38. Gonzalez, M. and Fall, A., 1998. The approach to self-preservation of scalar fluctuations decay in isotropic turbulence. Physics of Fluids, 10(3), pp.654-661.
39. Gregg, M.C., 1987. Diapycnal mixing in the thermocline: A review. Journal of Geophysical Research: Oceans, 92(C5), pp.5249-5286.
40. Grzelak, J.O.A.N.N.A. and Wierciński, Z.Y.G.M.U.N.T., 2015. The decay power law in turbulence generated by grids. Transactions of the Institute of Fluid-Flow Machinery.
41. Hall, I.R., Starr, A., Hemming, S.R., Barker, S., van der Lubbe, J., Cartagena Sierra, A., Berke, M.A., Gruetzner, J., Jiménez-Espejo, F.J.J., Knorr, G. and LeVay, L., 2019. Surface and deep-water variability on the southern Agulhas Plateau: Interhemispheric links over the past 2 Ma. AGUFM, 2019, pp.PP52A-05.
42. Hearst, R.J. and Lavoie, P., 2014. Decay of turbulence generated by a square-fractal-element grid. Journal of Fluid Mechanics, 741, pp.567-584.
43. Hicks, B.B. and Liss, P.S., 1976. Transfer of SO2 and other reactive gases across the air—sea interface. Tellus, 28(4), pp.348-354.
44. Hoult, D.P., 1972. Oil spreading on the sea. Annual Review of Fluid Mechanics, 4(1), pp.341-368.
45. Ikehara, M., Crosta, X. and Manoj, M.C., 2017. Impact of the Agulhas Return Current on the glacial Subantarctic region in the South Indian Ocean. AGUFM, 2017, pp.PP51A-1056.
46. Inoue, R., Gregg, M.C. and Harcourt, R.R., 2010. Mixing rates across the Gulf Stream, part 1: On the formation of Eighteen Degree Water. Journal of Marine Research, 68(5), pp.643-671.

47. Jaeger, G.S. and Mahadevan, A., 2018. Submesoscale-selective compensation of fronts in a salinity-stratified ocean. Science advances, 4(2), p.e1701504.
48. Janajrah M., Calay R. K.J., Lewis A.P. Holdo, A.E., and Bardan O., 2009. The Effect of the Physical Properties of Water Surface on Initial Wind-Waves Generation Mechanism at Low Wind In the Seventh Asia-Pacific Conference on Wind Engineering, November 8-12, 2009, Taipei, Taiwan.
49. Jones, I.S. and Kenney, B.C., 1977. The scaling of velocity fluctuations in the surface mixed layer. Journal of Geophysical Research, 82(9), pp.1392-1396.
50. Kahma, K.K. and Donelan, M.A., 1988. A laboratory study of the minimum wind speed for wind wave generation. Journal of Fluid Mechanics, 192, pp.339-364.
51. Kim, J. and Moin, P., 1989. Transport of passive scalars in a turbulent channel flow. In Turbulent Shear Flows 6 (pp. 85-96). Springer, Berlin, Heidelberg.
52. Kitaigorodskii, S.A., Donelan, M.A., Lumley, J.L. and Terray, E.A., 1983. Wave-turbulence interactions in the upper ocean. part ii. statistical characteristics of wave and turbulent components of the random velocity field in the marine surface layer. Journal of Physical Oceanography, 13(11), pp.1988-1999.
53. Konda, M., Ichikawa, H., Tomita, H. and Cronin, M.F., 2010. Surface heat flux variations across the Kuroshio Extension as observed by surface flux buoys. Journal of climate, 23(19), pp.5206-5221.
54. Kularatne, S. and Pattiaratchi, C., 2008. Turbulent kinetic energy and sediment resuspension due to wave groups. Continental Shelf Research, 28(6), pp.726-736.
55. Kurian, T. and Fransson, J.H., 2009. Grid-generated turbulence revisited. Fluid dynamics research, 41(2), p.021403.
56. Lamont, J.C. and Scott, D.S., 1970. An eddy cell model of mass transfer into the surface of a turbulent liquid. AIChE Journal, 16(4), pp.513-519.
57. Li, S., Li, M., Gerbi, G.P. and Song, J.B., 2013. Roles of breaking waves and Langmuir circulation in the surface boundary layer of a coastal ocean. Journal of Geophysical Research: Oceans, 118(10), pp.5173-5187.
58. Lin, S.C. and Lin, S.C., 1973. Study of strong temperature mixing in subsonic grid turbulence. The Physics of Fluids, 16(10), pp.1587-1598.

59. Liu, Y., Yu, L. and Chen, G., 2020. Characterization of Sea Surface Temperature and Air-Sea Heat Flux Anomalies Associated With Mesoscale Eddies in the South China Sea. Journal of Geophysical Research: Oceans, 125(4), p.e2019JC015470.
60. Lombardo, C.P. and Gregg, M.C., 1989. Similarity scaling of viscous and thermal dissipation in a convecting surface boundary layer. Journal of Geophysical Research: Oceans, 94(C5), pp.6273-6284.
61. Lueck, R.G., Hertzman, O. and Osborn, T.R., 1977. The spectral response of thermistors. Deep Sea Research, 24(10), pp.951-970.
62. Lueck, R.G., Wolk, F. and Yamazaki, H., 2002. Oceanic velocity microstructure measurements in the 20th century. Journal of Oceanography, 58(1), pp.153-174.
63. Luo, H., Bracco, A., Cardona, Y. and McWilliams, J.C., 2016. Submesoscale circulation in the northern Gulf of Mexico: Surface processes and the impact of the freshwater river input. Ocean Modelling, 101, pp.68-82.
64. McDougall, T.J., Jackett, D.R., Wright, D.G. and Feistel, R., 2003. Accurate and computationally efficient algorithms for potential temperature and density of seawater. Journal of Atmospheric and Oceanic Technology, 20(5), pp.730-741.
65. McWilliams, J.C., 2016. Submesoscale currents in the ocean. Proceedings of the Royal Society A: Mathematical, Physical and Engineering Sciences, 472(2189), p.20160117.
66. Mills Jr, R.R., Kistler, A.L., O'brien, V. and Corrsin, S., 1958. Turbulence and temperature fluctuations behind a heated grid.
67. Macías, D., Rodríguez-Santana, Á., Ramírez-Romero, E., Bruno, M., Pelegrí Llopart, J.L., Sangrá Inciarte, P., Aguiar González, M.B. and García, C.M., 2013. Turbulence as a driver for vertical plankton distribution in the subsurface upper ocean. Scientia Marina.
68. Mohamed, M.S. and Larue, J.C., 1990. The decay power law in grid-generated turbulence. Journal of Fluid Mechanics, 219, pp.195-214.
69. Monismith, S.G. and MacIntyre, S., 2010. The surface mixed layer in lakes and reservoirs. Biogeochemistry of inland waters. Elsevier, San Diego, pp.207-221.

70. Moum, J.N., 1996. Energy-containing scales of turbulence in the ocean thermocline. Journal of Geophysical Research: Oceans, 101(C6), pp.14095-14109.
71. Murzyn, F. and Bélorgey, M., 2005. Experimental investigation of the grid-generated turbulence features in a free surface flow. Experimental thermal and fluid science, 29(8), pp.925-935.
72. Nagai, T., Tandon, A., Yamazaki, H. and Doubell, M.J., 2009. Evidence of enhanced turbulent dissipation in the frontogenetic Kuroshio Front thermocline. Geophysical research letters, 36(12).
73. Nissanka, I.D. and Yapa, P.D., 2018. Calculation of oil droplet size distribution in ocean oil spills: A review. Marine pollution bulletin, 135, pp.723-734.
74. Oakey, N.S. and Elliott, J.A., 1977. Vertical temperature gradient structure across the Gulf Stream. Journal of Geophysical Research, 82(9), pp.1369-1380.Oakey, N.S., 1982. Determination of the rate of dissipation of turbulent energy from simultaneous temperature and velocity shear microstructure measurements. Journal of Physical Oceanography, 12(3), pp.256-271.
75. O'Neill, L.W., Haack, T., Chelton, D.B. and Skyllingstad, E., 2017. The Gulf Stream convergence zone in the time-mean winds. Journal of the Atmospheric Sciences, 74(7), pp.2383-2412.
76. Osborn, T.R., 1974. Vertical profiling of velocity microstructure. Journal of Physical Oceanography, 4(1), pp.109-115.
77. Osborn, T.R. and Cox, C.S., 1972. Oceanic fine structure. Geophysical & Astrophysical Fluid Dynamics, 3(1), pp.321-345.
78. Patterson, G. and Kachinjika, O., 1993. Effect of wind-induced mixing on the vertical distribution of nutrients and phytoplankton in Lake Malawi. Internationale Vereinigung für theoretische und angewandte Limnologie: Verhandlungen, 25(2), pp.872-876.
79. Pearman, J.K., Ellis, J., Irigoien, X., Sarma, Y.V.B., Jones, B.H. and Carvalho, S., 2017. Microbial planktonic communities in the Red Sea: high levels of spatial and temporal variability shaped by nutrient availability and turbulence. Scientific Reports, 7(1), pp.1-15.
80. Pécseli, H.L., Trulsen, J.K., Stiansen, J.E., Sundby, S. and Fossum, P., 2019. Feeding of plankton in turbulent oceans and lakes. Limnology and Oceanography, 64(3), pp.1034-1046.

81. Pereira, R., Ashton, I., Sabbaghzadeh, B., Shutler, J.D. and Upstill-Goddard, R.C., 2018. Reduced air–sea CO 2 exchange in the Atlantic Ocean due to biological surfactants. Nature Geoscience, p.1.
82. Petrenko, A.A., Doglioli, A.M., Nencioli, F., Kersalé, M., Hu, Z. and d'Ovidio, F., 2017. A review of the LATEX project: mesoscale to submesoscale processes in a coastal environment. Ocean Dynamics, 67(3-4), pp.513-533.
83. Pinker, R.T., Bentamy, A., Katsaros, K.B., Ma, Y. and Li, C., 2014. Estimates of net heat fluxes over the Atlantic Ocean. Journal of Geophysical Research: Oceans, 119(1), pp.410-427.
84. Platt, T., 1972, March. Local phytoplankton abundance and turbulence. In Deep Sea Research and Oceanographic Abstracts (Vol. 19, No. 3, pp. 183-187). Elsevier.
85. Qiao, F., Yuan, Y., Deng, J., Dai, D. and Song, Z., 2016. Wave–turbulence interaction-induced vertical mixing and its effects in ocean and climate models. Philosophical Transactions of the Royal Society A: Mathematical, Physical and Engineering Sciences, 374(2065), p.20150201.
86. Ruddick, B., Walsh, D. and Oakey, N., 1997. Variations in apparent mixing efficiency in the North Atlantic Central Water. Journal of Physical Oceanography, 27(12), pp.2589-2605.
87. Roll, H.U., 1951. Neue Messungen zur Entstehung von Wasserwellen durch Wind. Ann. Met, 4, pp.269-286.
88. Rothschild, B.J. and Osborn, T.R., 1988. Small-scale turbulence and plankton contact rates. Journal of plankton Research, 10(3), pp.465-474.
89. Sa, J.Y. and Kwak, D., 1997. A numerical method for incompressible flow with heat transfer.
90. Seuront, L., Tanaka, Y., Katano, T., Sugiyama, M., Watanabe, Y., Shimaraev, M.N. and Drucker, V.V., 2020. Intermittency in wind-generated turbulence in Lake Baikal: implications for biophysical couplings in the plankton. Limnology and Freshwater Biology, pp.693-694.
91. Shao, M., Ortiz-Suslow, D.G., Haus, B.K., Lund, B., Williams, N.J., Özgökmen, T.M., Laxague, N.J., Horstmann, J. and Klymak, J.M., 2019. The variability of winds and fluxes observed near submesoscale fronts. Journal of Geophysical Research: Oceans, 124(11), pp.7756-7780.

92. Shaw, W.J., Stanton, T.P., McPhee, M.G., Morison, J.H. and Martinson, D.G., 2009. Role of the upper ocean in the energy budget of Arctic sea ice during SHEBA. Journal of Geophysical Research: Oceans, 114(C6).
93. Smith, J.A., 2020. A Comparison of Two Methods Using Thorpe Sorting to Estimate Mixing. Journal of Atmospheric and Oceanic Technology, 37(1), pp.3-15.
94. Speziale, C.G. and Bernard, P.S., 1992. The energy decay in self-preserving isotropic turbulence revisited. Journal of Fluid Mechanics, 241, pp.645-667.
95. Sreenivasan, K.R., Tavoularis, S., Henry, R. and Corrsin, S., 1980. Temperature fluctuations and scales in grid-generated turbulence. Journal of Fluid Mechanics, 100(3), pp.597-621.
96. Sun, D., Bracco, A., Barkan, R., Berta, M., Dauhajre, D., Molemaker, M.J., Choi, J., Liu, G., Griffa, A. and McWilliams, J.C., 2020. Diurnal cycling of submesoscale dynamics: Lagrangian implications in drifter observations and model simulations of the northern gulf of mexico. Journal of Physical Oceanography, 50(6), pp.1605-1623.
97. Sutherland, G., Ward, B. and Christensen, K.H., 2013. Wave-turbulence scaling in the Near-surface layer. Ocean Science, 9(4), pp.597-608.
98. Taguchi, B., Nakamura, H., Nonaka, M. and Xie, S.P., 2009. Influences of the Kuroshio/Oyashio Extensions on air–sea heat exchanges and storm-track activity as revealed in regional atmospheric model simulations for the 2003/04 cold season. Journal of Climate, 22(24), pp.6536-6560.
99. Tennekes, H., Lumley, J.L. and Lumley, J.L., 1972. A first course in turbulence. MIT press.
100. Terray, E.A., Donelan, M.A., Agrawal, Y.C., Drennan, W.M., Kahma, K.K., Williams, A.J., Hwang, P.A. and Kitaigorodskii, S.A., 1996. Estimates of kinetic energy dissipation under breaking waves. Journal of Physical Oceanography, 26(5), pp.792-807.
101. Tintore, J., La Violette, P.E., Blade, I. and Cruzado, A., 1988. A study of an intense density front in the eastern Alboran Sea: the Almeria–Oran front. Journal of Physical Oceanography, 18(10), pp.1384-1397.
102. Wang, Z., DiMarco, S.F. and Socolofsky, S.A., 2016. Turbulence measurements in the northern Gulf of Mexico: Application to the Deepwater Horizon oil spill on droplet dynamics. Deep Sea Research Part I: Oceanographic Research Papers, 109, pp.40-50.

103. Warhaft, Z. and Lumley, J.L., 1978. An experimental study of the decay of temperature fluctuations in grid-generated turbulence. Journal of Fluid Mechanics, 88(4), pp.659-684.

104. Wells, A.J., Cenedese, C., Farrar, J.T. and Zappa, C.J., 2009. Variations in ocean surface temperature due to near-surface flow: Straining the cool skin layer. Journal of physical oceanography, 39(11), pp.2685-2710.

105. Zhou, T., Antonia, R.A., Danaila, L. and Anselmet, F., 2000. Transport equations for the mean energy and temperature dissipation rates in grid turbulence. Experiments in Fluids, 28(2), pp.143-151.

106. Zieliński, M., Fortuniak, K., Pawlak, W. and Siedlecki, M., 2018. Long-term Turbulent Sensible-Heat-Flux Measurements with a Large-Aperture Scintillometer in the Centre of Łódź, Central Poland. Boundary-Layer Meteorology, 167(3), pp.469-492.

107. Xue, H. and Mellor, G., 1993. Instability of the Gulf Stream front in the South Atlantic Bight. Journal of physical oceanography, 23(11), pp.2326-2350.

LIST OF APPENDICES

APPENDIX PAGE

Appendix A:

Steady and spatially decaying background turbulence-grid generated-turbulence

Batchelor and Townsend (1948) and Warhaft and Lumley (1978) observed that the mean turbulent kinetic energy, $< q^2 > \sim < u'^2 > + < v'^2 > + < w'^2 >$ and temperature variance, $<\theta^2>$, decay with distance from the grid. Where U is the flow velocity in the streamwise direction, x, and can be represented by $U =< U > + u'$, (see Fig. 2). Here $< U >$ is the mean flow velocity and u' is the fluctuation part of velocity. Similarly, for the other velocity components $V =< V > + v'$, in the y-direction, and $W =< W > + w'$, in the z-direction. The water temperature is $T =< T > + \theta$, where $< T >$ is mean temperature value and θ is fluctuation part of the temperature.

Grid-generated turbulence is one of the simplest turbulence flows that creates an isotropic and homogeneous turbulence ($\partial/\partial t = U\partial/\partial x$) in the streamwise direction. The isotropic turbulence has interested scientists which has let them to research about it experimentally (Warhaft 1983, Itsweire et al., 1986 and Isaza et al., 2014), theoretically (Wyngaard 1970) and numerically (Nagata et al., 2008 and Djenidi et al., 2014 and 2015). The mean turbulent energy ($<q^2>$) and temperature variance ($<\theta^2>$) decay in self-preservation grid-generated turbulence have been studied for decades. One of the first studies about the energy decay in isotropic turbulence was done by Batchelor (1948). Speziale et al., 1992 presented that the turbulent kinetic energy decay is equal to $<q^2> \sim t^{-1}$ or equivalently $<q^2> \sim x^{-1}$ (power law decay) for high Taylor microscale Reynolds number ($Re_\lambda = u' \lambda / \nu$, where u' is the fluctuation part of velocity, λ is Taylor microscale and ν is kinematic viscosity). He expressed that the power law decay $<q^2> \sim t^{-\alpha}$ with an exponent $\alpha > 1$ is achieved in the limit as $t \rightarrow \infty$ and a vanishingly small turbulence Reynolds number. In other

words, n >1, when Re_λ is neither very high or very small (Transition region). George (1992) claimed that he found a complete self-preserving solution which is valid for all Reynolds numbers in which α is determined by the initial condition. Later, Antonio et al., (1998) showed the value of n = 1.28 and more recently, Hearst et al. (2014) found the value of n to be about 1.37 and 1.39. In addition to energy decay, the decay rate of scalar fluctuation has been researched by scientists. Warhaft et al., (1978) showed that the temperature fluctuation decay rate, produced by heating grid, depends on the wave number at which the temperature spectrum peaks. By changing the grid heating, the location of the peak of the three dimensional temperature spectrum changes; however, the peak of the velocity spectrum does not move (Newman et al., 1997). Gonzalez et al., (1977), from a fixed point analysis, identified the existence of two asymptotic self-preserving regimes. The first regime corresponds to the final period of decay (Vanishingly small Reynolds number) which is determined by the initial value of enstrophy destruction coefficient. The other regime relates to high Reynolds number that depends on the enstrophy destruction and its initial value, velocity derivative skewness and the mixed derivative skewness coefficients. Gonzalez et al., (1977) expressed that the self-preserving regime for high Reynolds number is not universal for temperature decay rate, whereas, the energy decay has universality for high Reynolds number. It means that the value of m exhibits a large scatter in comparison to the value of n. Lin et al., (1973) reached to the values of between m = 2.53 to 3.09 for different heating power. The experimental results for Milles et al., (1958) and Sreenivasan et al., (1980) showed the value of m= 0.87 and m= 3.1, respectively.

The governing equations for the evolution of mean turbulent kinetic energy and the temperature variance in the homogeneous and isotropic shear flow are (Pope 2001)

$$\frac{dq^2}{2\,dt} \approx P - \varepsilon \quad \text{(A1)}$$

$$\frac{d\theta^2}{2\,dt} \approx P_\theta - \chi \quad \text{(A2)}$$

Here P is the turbulent kinetic energy production by the mean flow and for a shear flow we have $P \approx -\langle u_i' u_j' \rangle \frac{\partial \langle U_i \rangle}{\partial x_j}$, and P_θ is temperature variance production rate, $P_\theta \approx -\langle u_i' \theta_j \rangle \frac{\partial \langle T_i \rangle}{\partial x_j}$, while i and j=1, 2 and 3 corresponding to x, y and z coordinates, respectively. In the grid-generated turbulence, the production terms equal to $P = 0$ and $P_\theta = 0$ due to the absence of the mean velocity and mean temperature gradient through the streamwise direction. Downstream from the grid, the spatial and temporal derivatives can be related (Murzyn and Belorgey 2004) as:

$$\partial/\partial t = -\langle U \rangle \partial/\partial x \quad \text{(A3)}$$

From Eqs. A1 and A2 and with the aid of the Eq. (A3), the mean turbulent kinetic energy, $\langle q^2 \rangle$, and temperature variance, $\langle \theta^2 \rangle$, in grid-generated turbulence, can be expressed as (Zhou et al. 2000):

$$-\frac{\langle U \rangle}{2} \frac{d\langle q^2 \rangle}{dx} \approx \langle \varepsilon \rangle \quad \text{(A4)}$$

and

$$-\frac{\langle U \rangle}{2} \frac{d\langle \theta^2 \rangle}{dx} \approx \langle \chi \rangle \quad \text{(A5)}$$

Numerous experiments (Batchelor and Townsend 1948, Comte-Bellot and Corrsin 1996 and Zhou et al., 2000) suggest that the downstream decay of the mean turbulent kinetic energy and temperature variance behind the grids are:

$$\langle q^2 \rangle \approx A\,(x - x_0)^{-n} \quad \text{(A6)}$$

and

$$\langle \theta^2 \rangle \approx B(x - x_0')^{-m} \quad \text{(A7)}$$

where n and m are the exponents of the mean turbulent kinetic energy and temperature variances respectively. The constants A and B depend on the grid geometry and are typically determined empirically. The horizontal distance from the turbulence generating grid in the streamwise direction is x while x_0 is the virtual origin of the grid-generated turbulence and x_0' is the virtual origin of the heater grid. Sreenivasan et al. (1980) found that in their experiment, values of x_0 and x_0' are about 3M, M is grid mesh size. The value of n changes only ±2 % by varying x_0 /M by ±1 (Zhou et al. 2000). in our experiment we assume $x_0 = 0$ and $x_0' = 0$.

By substituting equations A6 and A7 into A4 and A5, the power-law decay exponent for TKED and TD are the following:

$$< \varepsilon > \approx \frac{n<U>A}{2} x^{-(n+1)} \tag{A8}$$

and

$$< \chi > \approx \frac{n<U>B}{2} x^{-(m+1)} \tag{A9}$$

Speziale and Bernard (1992) found that the mean turbulent kinetic energy decay is proportional to $<q^2> \sim t^{-1}$ or equivalently $<q^2> \sim x^{-1}$, at large Reynolds number, $R_t = q^4/4\nu\epsilon$ >1000 (Gonzalez and Fall 1998). Later, Antonia et al. (1998) showed the value of $n = 1.28$ and more recently, Hearst and Lavoie (2014) found the value of n = 1.37 and 1.39 behind a square-fractal-element grid.

Appendix B:

Free convection flow and associated vertical heat flux

The transfer of heat from water to air resulted in thermal convection in our experiment as salinity was approximately zero within the water depth. Convection affects the vertical transport of heat, momentum, and other properties within the upper ocean boundary layer (Soloviev et al., 2001). Fredriksson et al. (2016) have modeled the convection, and found that the convection resulted in a sharp change of TKED at a depth of $z \approx 0.015$ m up to the water surface for the Rayleigh number of $\mathrm{Ra} = \frac{B_0 L^4}{\alpha^2 \vartheta} = 5*10^8$ (Fredriksson et al., 2016), where L is a characteristic length. The surface bouyancy flux $B_0 = -{c_p}^{-1}\rho^{-1}g\alpha Q + \rho^{-1}g\beta sE$ (Zahariev and Garrett 1997), where c_p is the specific heat of water, ρ is water density, g is gravity, α is the thermal expansion coefficient of water, β is the coefficient of salinity expansion, s is the surface salinity, and E is evaporation rate. The buoyancy length scale is defined as $L_0 = k{u_*}^3/B_0$, where u_* is the surface friction velocity, by Obukhov in the 1950s. Shortly thereafter, Monin and Obukhov (1954) suggested the stability parameter, $\xi = z/L_0$, to characterize the relative importance of the shear-production of turbulence, and bouyancy production in the planetary boundary layer (Markowski et al., 2019 and Optics et al., 2016). The Monin-Oboukhov theory is applicable to the ocean boundary layer as the atmospheric and oceanic turbulent boundary layers are analogs (Soloviev et al., 2001). Priestley (1955) showed that for a depth of $z > |0.03L_0|$ the shear-production of turbulence can be neglected compared to the convective turbulence.

To understand the convection effects in the surface boundary layer, we calculated the turbulent vertical heat flux $< w'\theta >$. We followed the Osborn and Cox (1972) approach to determine the value of $< w'\theta >$.

Conservation of heat within an incompressible fluid without a heat source can be described by the advection-diffusion equation (Kim and Moin, 1989) as:

$$\frac{\partial T}{\partial t} + U_i \frac{\partial T}{\partial x_i} = K_\theta \frac{\partial^2 T}{\partial {x_i}^2} \tag{B1}$$

After performing the Reynolds decomposition and with the Reynolds average denoted as < >, Eq. B1 can be written as:

$$\frac{\partial <T>}{\partial t} + < U_i > \frac{\partial <T>}{\partial x_i} + \frac{\partial}{\partial x_i} < u_i'\theta > = K_\theta \frac{\partial^2 <T>}{\partial {x_i}^2} \tag{B2}$$

Subtracting equations B2 from B1, the budget of turbulence thermal variance becomes:

$$\frac{\partial \theta}{\partial t} + u_i' \frac{\partial <T>}{\partial x_i} + u_i' \frac{\partial \theta}{\partial x_i} + < U_i > \frac{\partial \theta}{\partial x_i} - \frac{\partial}{\partial x_i} < u_i'\theta > = K_\theta \nabla^2 \theta \tag{B3}$$

Eq. B3 is multiplied by θ and averaged to yield (Gregg 1987):

$$\frac{\partial < \theta^2 >}{\partial t} + 2 < u_i'\theta > \frac{\partial < T >}{\partial x_i} + < U_i > \frac{\partial}{\partial x_i} < \theta^2 > + \frac{\partial}{\partial x_i} < u_i'\theta^2 >$$

$$= K_\theta \nabla^2 < \theta^2 > - 2K_\theta < \left(\frac{\partial \theta}{\partial x_i}\right)^2 > \tag{B4}$$

For steady and homogeneous turbulence and retaining only vertical dependence, Eq. B4 reduces to (Ruddick et al. 1997):

$$< w'\theta > \frac{\partial <T>}{\partial z} = - K_\theta < (\nabla \theta)^2 > \tag{B5}$$

Eq. B5 relates the small-scale temperature fluctuation to the vertical turbulent heat flow. As $\varepsilon_\theta = 2K_\theta < (\nabla\theta)^2 >$, the Eq. 13 can be expressed as (Ruddick et al. 1997):

$$\frac{1}{2}\chi = -<w'\theta>\frac{\partial<T>}{\partial z} \quad \text{(B6)}$$

In our experiment, the value of the vertical turbulent heat flux, $<w'\theta>$, can be estimated as we measured the values of ε_θ and $\frac{\partial<T>}{\partial z}$. Also, the vertical temperature gradient, $\frac{\partial<T>}{\partial z}$, could help to quantify the net vertical heat flux, Q, at the surface. The net vertical heat flux Q generates a vertical temperature gradient and they have a linear relation as (Wells et al., 2009)

$$-\rho c_p K_\theta \frac{\partial<T>}{\partial z} = Q \quad \text{(B7)}$$

Where c_p is specific heat capacity and $Q = Q_r + Q_s + Q_l$. Here Q_r is a radiative component of air-water heat flux, Q_s and Q_l are evaporative and sensible heat flux components, respectively. Eq. B6 shows that the vertical near surface temperature gradient is proportional to the heat flux at the surface.

Appendix C:

Wave boundary layer

The base of our understanding of the vertical turbulence variability within surface boundary layers in the ocean is mainly based on turbulent flow studies over solid wall-layer turbulence with the corresponding ‘‘law of the wall’’ (Kiataigorodskii et al., 1983 and Gargett 1989), where the wind stress is assumed to be constant across the air-sea interface. For a steady-state solution and ignoring buoyancy, the vertical TKED equals to (Pope, 2000):

$$\varepsilon = \frac{{u^*}^3}{(kz)} \tag{C1}$$

Eq. C1 is the law of the wall where von Karman’s constant is k=0.41 and u^* is friction velocity. Agrawal et al. 1992 observed an enhanced dissipation rate of 1 to 2 orders of magnitude larger than predicted by the law of the wall. Terray et al. (1996) suggested enhanced values for the TKED relative to the law of the wall in the upper ocean, and this enhanced vertical TKED was a result of the wind-wave field. They reported that the vertical TKED had an enhanced uniform value due to the breaking waves from the water surface to a depth of $z = 0.6H_s$, here $H_s$is a significant wave height. Anis and Moum (1995) reported an enhanced value of TKED due to breaking waves and wave turbulence interaction. They observed that the vertical TKED profiles decay exponentially with depth, and introduced a corresponding TKED as $\varepsilon = 2K\alpha_1 u_{s0} {u_*}^3 * e^{-2Kz}$. Here α_1 is a dimensionless constant, the wave Stoke drift at the ocean surface is u_{s0}, and K is the wave number.

Terray et al.(1996) suggested enhanced values for the TKED relative to the LOW in the upper ocean, and this enhanced vertical TKED resulted from the wind-wave field. They reported three vertical layers (Terray et al., 1996):

$$\varepsilon_{Wave}(z) = \begin{cases} 0.3\alpha_1 (\frac{u_*^3}{H_s})(\frac{z_b}{H_s})^{-2} & z < z_b \\ 0.3\alpha_1 (\frac{u_*^3}{H_s})(\frac{z}{H_s})^{-2} & z_b \leqslant z \leqslant z_t \\ \frac{u_*^3}{(kz)} & z > z_t \end{cases} \quad \text{(C2)}$$

The vertical TKED had a constant uniform value due to the breaking waves from the water surface to a depth of ''breaking depth'', $z_b = 0.6H_s$, here H_s is a significant wave height. For simplicity, the wave height $H = 2 < \eta >$ (Table 1) and significant wave height H_s are considered equal in our experiment. In this layer, the TKED is assumed to be an order of magnitude larger than the LOW. Bellow the breaking layer, the TKED is decreased downward to ''transition depth'', $z_t = 0.3H_s \frac{\bar{c}}{u_{a*}}$, and bellow that the TKED follows the behavior of the LOW. $\bar{c}$ is an effective wave speed that it is determined to be dominated by the short waves and equals to $\bar{c} \approx 1$ m/s (Gemmrich et. al., 2010). α_1 is defined as a function of wave age $\frac{c_p}{u_{a*}}$, where c_p is the phase velocity of the waves.

$$\alpha_1 = \begin{cases} 0.5\left(\frac{c_p}{u_{a*}}\right)(\frac{\rho}{\rho_a})^{\frac{1}{2}} & \frac{c_p}{u_{a*}} \leqslant 11 \\ 12(\frac{c_p}{u_{a*}})^{-\frac{1}{3}}(\frac{\rho}{\rho_a})^{\frac{1}{2}} & \frac{c_p}{u_{a*}} > 11 \end{cases} \quad \text{(C3)}$$

Appendix D:

Modified grid-generated turbulence model

We postulate that in the presence of external heat sources in our experiment there is the following relationship between total water temperature variance (θ^2) created by grid (θ_{grid}^2) and external heat flux ($\theta_{surface}^2$) :

$$\theta^2 = \theta_{grid}^2 + \theta_{surface}^2 \quad \text{(D1)}$$

The transport equation (Eq. D1) of the temperature variance can then be rewritten as follows:

$$-\frac{<U>}{2}\frac{d<\theta_{grid}^2>}{dx} \approx < \chi > + \frac{<U>}{2}\frac{d<\theta_{surface}^2>}{dx} \quad \text{(D2)}$$

Similaryly for the TKED, in the presence of additional source of velocity fluctuation (for example due to uneven walls), we can modify Eq. A4 to become

$$-\frac{<U>}{2}\frac{d<q_{grid}^2>}{dx} \approx < \varepsilon > + (\frac{<U>}{2}\frac{d<q_{Added}^2>}{dx}) \quad \text{(D3)}$$

Here $< q_{grid}^2 >$ and $< q_{Added}^2 >$ is the mean turbulent kinetic energy created by the grid and either wall of the tank or the convection, respectively.

Appendix E:

Spectrum

Spectrum function (S (ω), ω is angular frequency and equals to $\omega = 2\pi f$ (f is frequency)) of a time series data, F(t), shows the strength of variations as a function of frequency. For calculating the power spectrum, the autocorrelation of a variable, x(t), should be calculated.

$$R(t_1, t_2) = \langle F(t_1)F(t_2)\rangle \quad \text{(E1)}$$

Where t_1 and t_2 are two times. In the case of wide-sense stationary random processes, the autocorrelation is only related to the time difference ($\tau = t_2 - t_1$).

$$R(\tau) = \langle F(t)F(t+\tau)\rangle \quad \text{(E2)}$$

Let F(ω) denote the Fourier transform of the autocorrelation function $R(\tau)$

$$F(\omega) = \frac{1}{2\pi}\int_{-\infty}^{\infty} R(\tau)\, e^{-i\omega\tau}\, d\tau \quad \text{(E3)}$$

For τ = 0, the F(ω) equals to spectrum function

$$S(\omega) = F_{\tau=0}(\omega) \quad \text{(E4)}$$

Since the structure of turbulence parameters are more interested in space rather than time, we need to calculate autocorrelation in space.

The autocorrelation in space is calculated through an analogy way of the autocorrelation in time. Therefore, the spatial autocorrelation for two points, x_1 and $x_2 = x_1 + x_d$ (xd is the difference between two points), defines as

$$R(x_0) = \langle F(t, x_1)F(t, x_1 + x_d)\rangle \quad \text{(E5)}$$

Spectrum function (S (K), $K$is wave number and equals to $K = 2\pi\lambda$ (λ is wave length)) can be formulated as

$$F(K) = \frac{1}{2\pi}\int_{-\infty}^{\infty} R(x_d)\, e^{-iKx_d}\, d \qquad \text{(E6)}$$

For x_d = 0, the F(ω) equals to spectrum function

$$S\,(\omega) = F_{x_d=0}(\omega) \qquad \text{(E7)}$$

Appendix F:

Vertical Microstructure Profiler (VMP) – 200

The VMP_200 (is built by Rockland Scientific International Inc. (RSI)) is an instrument designed to record the ocean's two main physical parameters, temperature variability, and velocity shear that. It measures the parameter on vertical scales of less than a millimeter. In addition, the instrument has the ability to measure other parameters of the ocean, like conductivity and pressure. The VMP-200 was designed for depth between 0-500 m. It has 2 shear probes (figure 13), 1 thermistor probe (figure 14), and 1 conductivity probe.

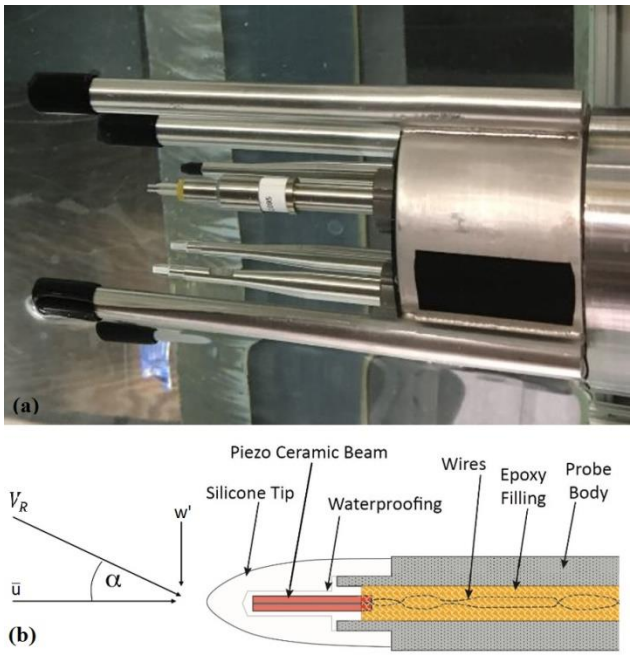

Figure 13. Figure (a) shows the four probes of the VMP and a schematic of the shear probe and angle of attack presents in figure (b) (www.rocklandscientific.com).

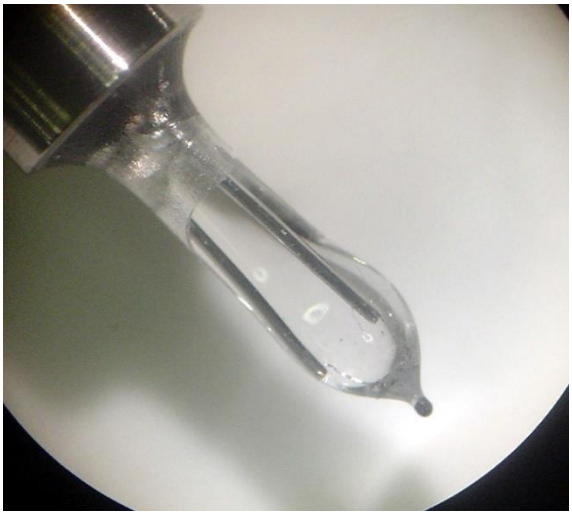

Figure. 14 The image of the tip of the thermistor probe (www.rocklandscientific.com).

The shear probe measures cross-stream velocity fluctuation to its data collecting direction. The probe is an air-foil shear probe. The length of the shear probe is 13 mm long that half of it is anchored by covering stainless steel sting, and the other half will generate a charge when it bends by pressure created by cross-stream velocity fluctuation. Imagine there is a cross-stream fluctuation, w', and a mean axial velocity $< U >$ that passes the probe tip. The resultant of the velocities, V_R, creates an angle of attack, α which it is better not to increase more than 12 degree (See appendix C). The velocity components produce a lift force over the shear probe, and the charge produced by the probe is proportional to the lift force

$$F \sim \rho < U > w' \qquad \text{(F1)}$$

The capacitor changes the charge to the voltage, resulting in the velocity shear $(\frac{\partial w'}{\partial x})$ to be measured. Collecting data by VMP occurs in two manners. The first manner is when the VMP is moving through the water like when it falls down or rises up vertically through column water. The

other way is when the VMP is stationary, and flow passes the probe, such as the VMP mounted horizontally in the tank.

In General, the TKED (ε) is calculated by (Saarenrinne and Piirto 2000)

$$\varepsilon = \nu < \frac{\partial u_j'}{\partial x_i} (\frac{\partial u_i'}{\partial x_j} + \frac{\partial u_j'}{\partial x_i}) > \quad \text{(F2)}$$

For Homogeneous and isotropic turbulence, the relation is simplified to

$$\varepsilon \approx \frac{15}{2} \nu < (\frac{\partial w'}{\partial x})^2 > \quad \text{(F3)}$$

The equation can also be used for the other five components of shear ($\frac{\partial u'}{\partial z}$, $\frac{\partial u'}{\partial y}$, $\frac{\partial v'}{\partial x}$, $\frac{\partial v'}{\partial z}$, $\frac{\partial w'}{\partial y}$). On the other three components of the rate of strain ($\frac{\partial u'}{\partial x}$, $\frac{\partial v'}{\partial y}$, $\frac{\partial w'}{\partial z}$), the equation is applicable by increasing the numerical scale factor from $\frac{15}{2}$ to 15. As $< (\frac{\partial w'}{\partial x})^2 >$ equals to spectrum function; therefore the equation F3 can is rewritten to

$$\varepsilon \approx \frac{15}{2} \nu < (\frac{\partial w'}{\partial x})^2 > \approx \frac{15}{2} \nu \int_0^\infty \psi(K) dK \quad \text{(F4)}$$

Where K is wavenumber and $\psi(K)$ is the spectrum of velocity shear (see figure 15), $\frac{\partial w'}{\partial x}$.

The thermistor probe in the VMP measures the temperature variance and by having that the TD (ε_θ) will be measured. The TD (ε_θ) is given by (Bluteau et al., 2017)

$$\chi \approx 2K_\theta < (\nabla\theta)^2 > \quad \text{(F5)}$$

For isotrpic turbulence, the TD (ε_θ) is simplified to (Bluteau et al., 2017)

$$\chi \approx 6\, K_\theta < (\frac{\partial \theta}{\partial z})^2 > \quad \text{(F6)}$$

As $< (\frac{\partial \theta}{\partial z})^2 >$ equals to spectrum function; therefore the equation F3 is rewritten to (Bluteau et al. 2017 and Bogucki and Domaradzki 2012)

$$\chi \approx 6\, K_\theta < (\frac{\partial \theta}{\partial z})^2 > \approx\ 6\, K_\theta \int_0^\infty \Phi(K) dK \qquad \text{(F7)}$$

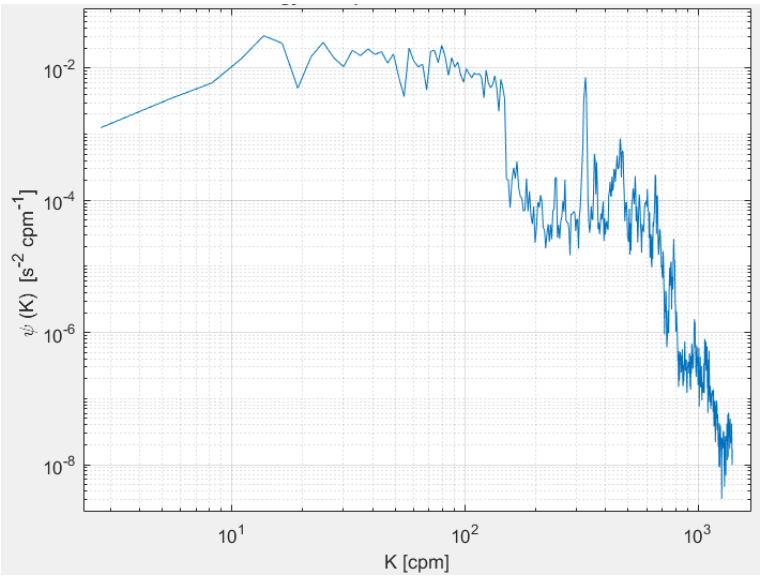

Fig.15 The velocity shear spectrum for the mean flow velocity of 0.183 m/s at the depth z= 0.05 m.

$\Phi(K)$ is one-sided temperature gradient spectral (see figure 16). For calculating the ε_θ A thermistor probe, which is a metal-oxide resistor, is mounted at the VMP. The metal-oxide resistor has a large negative temperature-coefficient of resistance ($\alpha \sim -0.04\, C^{-1}$) that makes them usable for detecting small temperature fluctuations. The PF07 thermistor (Figure 14) is usually used for the temperature sensor. The black dot at the tip of the probe is its sensing element (metal-oxide bead) with 180 μm diameter. The sensing tip is mounted into a glass substrate with a thickness of 50 μm. The bead is fused on to a bulbous glass substrate with a 2mm diameter that makes a rod of 10 mm length epoxied into a stainless sting. A single-pole response function (see Eq. F8) was used to correct the FP07 thermistor data (Lueck et al. 1977).

$$H^2(f) = \left(\frac{1}{1+(f/f_c)^2}\right)^2 \quad \text{(F8)}$$

Where $H(f)$ is the response function and the relationship between water temperature spectrum ($T_0(f)$) and observed water temperature spectrum ($T_m(f)$) is $H(f) = T_m(f) \,/\, T_0(f)$. f is the frequency and can be substituted by $f = < U > \hat{K}$ (where $\hat{K}$ is the cyclical wavenumber, $\hat{k} = K/2\pi$). f_c is filter cutoff frequency, which presents 3 db drop for a single-pole filter function. The cutoff frequency is related to mean current speed ($< U >$), $f_c = f_0 \ < U >^p$, where f_0 and p are thermistor dependent (Bogucki et al. 2012).

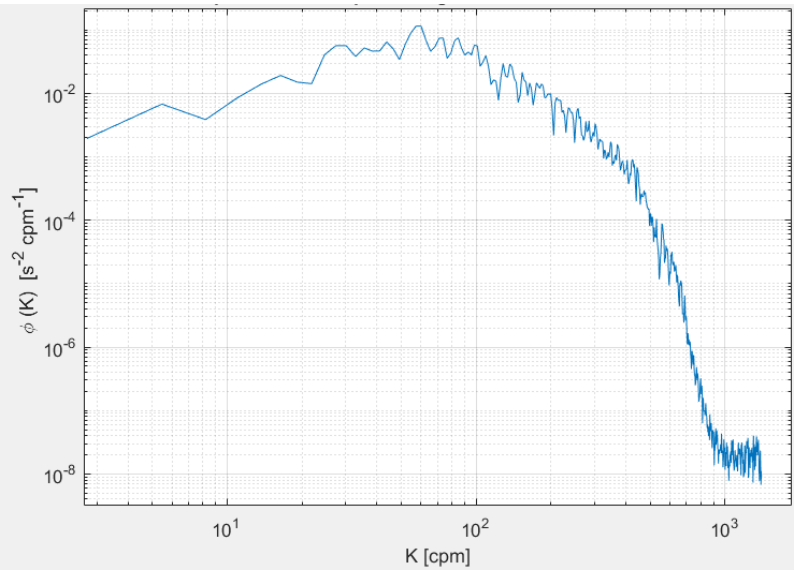

Fig.16 The temperature variance spectrum for the mean flow velocity of 0.183 m/s at the depth z= 0.05 m.

Appendix G:

Angle of attack:

In fluid dynamics, the angle of attack, α, (See figure 13 of appendix B) is the angle between the oncoming flow and a reference line on the body. In our experiment, the angle of attack is between the sensors and water flow passing the sensors, by increasing the angle of attack, the error of the instrument results increases. The experiment was conducted to determine the effects of angle of attack on the results. The experiment was done in the ASIST tank of RSMAS at the University of Miami (See figure 9). The tank set-up was the same as the power-law experiment. The velocity of the flow was 0.185 m/s, and the heater was full power. The VMP mounted at $x/M = 37$at the depth of x D = 25cm from the water surface. In the beginning, the VMP was horizontally, and then, the angle of the VMP and horizontal line (angle of attack) increased to 18.3 degrees.

By increasing the angle of attack up to 12 degree, the TKED is approximately constant (Figure 17). For the angle more than 12 degrees, the error starts to go up, and at the 18.3 degrees, the value of ε increases to 60 percent more than when the VMP is horizontal (α=0). The tip of the shear sensor is the sensitive element of the probe and measures the velocity shear. By passing the flow through the sensor, a boundary layer separation point creates over the probe stem, which makes extra turbulence at the boundary layer. When the angle of attack increases, the separation point created on the stem of the probe moves toward the tip of the probe. At the angle of 14, the tip starts to feel the separation point, and that is the reason there is a jump in results at this angle. Therefore, for having good results with less than 20 percent error, the angle of attack should be less than 14 degrees. For the scalar fluctuation, like temperature, the angle of attack does not affect results as much as the TKED because the velocity has a small effect on the temperature fluctuation.

Figure 18 shows that increasing the angle of attack causes a decrease in the ε_θ and by reaching to 18.3 degrees, the results decrease 25 percent. From 0 to 10 degree angle, the value of $\varepsilon_\theta/\varepsilon_{\theta 0}$ ($\varepsilon_{\theta 0}$ is TD when the VMP is in its initial position (horizontally), $\alpha = 0$) does not go less than 0.80 and the average is about 0.92 and for angle bigger than 10 degree, the average of $\varepsilon_\theta/\varepsilon_{\theta 0}$ reaches to 0.78. In general, when the angle of attack is less than 12, the results of shear and thermistor probe are reliable.

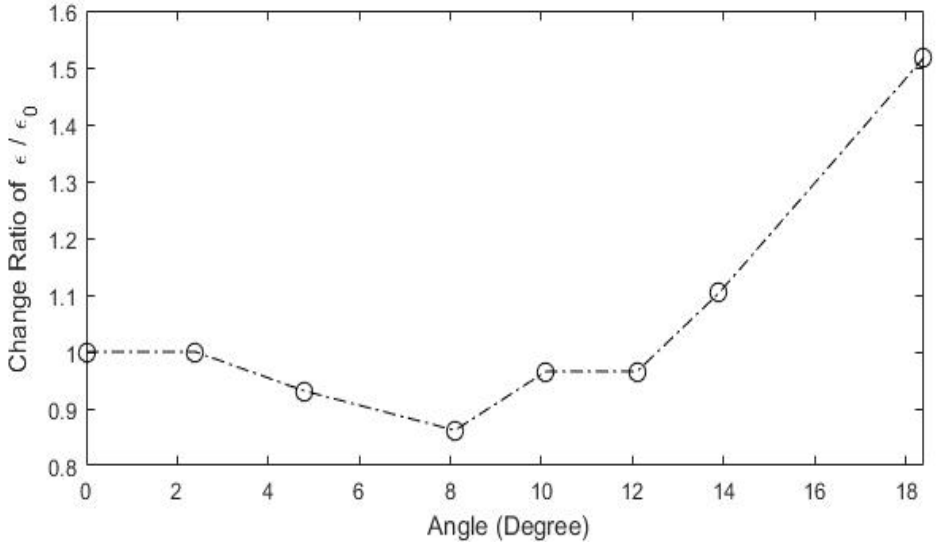

Fig. 17. The effect of the angle of attack on the ε is presented. The X-axis shows the angle of VMP toward the horizon and the Y-axis shows the change ratio of the ε by increasing the angle of attack. The ε_0 is the TKED at the angle of attack α=0.

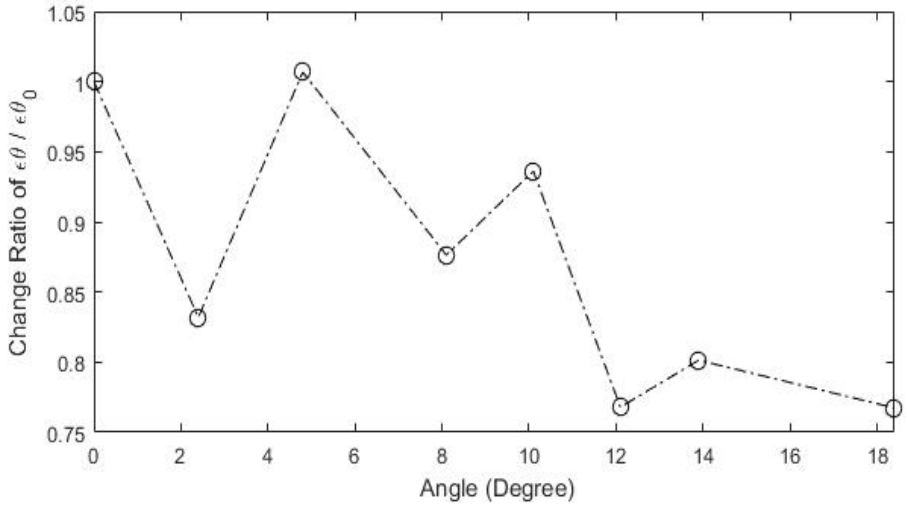

Fig. 18. shows the effects of angle of attack (VMP Angle) on the ε_θ. X-axis shows the angle of VMP toward the horizon, and Y-axis shows the change ratio of ε_θ by increasing the angle of attack. The $\varepsilon_{\theta 0}$is the TD at the angle of attack α=0.

Appendix H:

Gravity-capillary wave slope data:

A surface slope gauge is used to measure the 2D wave's surface slope. From below, a narrow vertical laser beam is emitted through the water. After touching the water surface, the laser beam refracts at an angle dependent on the instantaneous surface slope so that way the surface slope is measured.

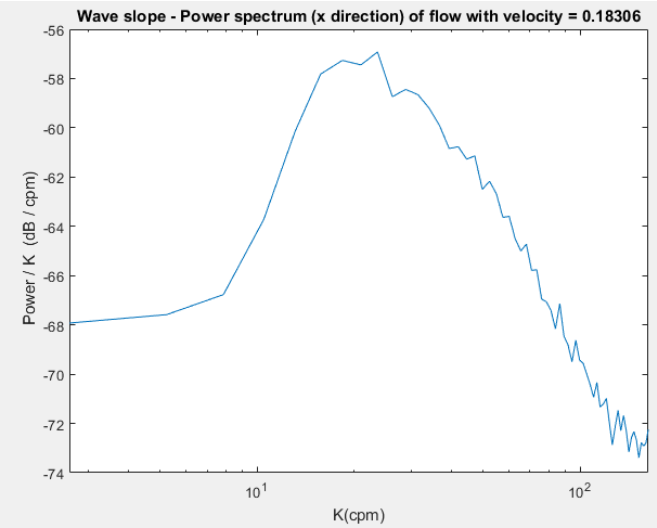

Fig. 19 The surface slope spectrum for the mean flow velocity of 0.183 m/s.

The 2D surface slope is presented in terms of the directional wavenumber spectrum P such that

$$\langle g^2 \rangle = \int_{-\infty}^{+\infty} \int_{-\infty}^{+\infty} P(K_x, K_y)\, dK_x dK_y = \int_0^{+\infty} \int_{-\pi}^{+\pi} P(K, \emptyset) K\, dK d\emptyset = \int_0^{+\infty} S(K) dK \qquad \text{(H1)}$$

Where $\langle g^2 \rangle$ is the mean square surface slope, $S(K)$ is omnidirectional slope spectrum, $k = \sqrt{K_x^2 + K_y^2}$ (k_x and K_y are wave number in x and y direction, respectively) and $\emptyset$ is azimuth angle.

In the present paper, the one-dimensional surface slope spectrum is calculated due to that the flow

moves through the x-direction and only K_x is important. The surface slope spectrum for flow velocity of 0.183 m/s is plotted in figure 19. The range of K = 18.35 – 23.6 cpm is considered as a maximum K due to wave instability.